

Study and application of solitary wave propagation at fractional order of time based on SPH method

Luyang Ma(马璐阳), Rahmatjan Imin(热合买提江·依明), and Azhar Halik(艾孜海尔·哈力克)

Citation: Chin. Phys. B, 2025, 34 (**5**): 050202. DOI: 10.1088/1674-1056/adbd2a
Journal homepage: http://cpb.iphy.ac.cn; http://iopscience.iop.org/cpb

What follows is a list of articles you may be interested in

Trajectory equations of interaction and evolution behaviors of a novel multi-soliton to a (2+1)-dimensional shallow water wave model

Xi-Yu Tan(谭茜宇) and Wei Tan(谭伟)
Chin. Phys. B, 2025, 34 (**4**): 040202. DOI: 10.1088/1674-1056/ada7da

New interaction solutions in Mel'nikov equation obtained by modulating the phase shift

Mi Chen(陈觅) and Zhen Wang(王振)
Chin. Phys. B, 2025, 34 (**4**): 040201. DOI: 10.1088/1674-1056/adaccb

Riemann-Hilbert approach to the higher-order Kaup-Newell equation on the half line

Hui Yu(于慧) and Ning Zhang(张宁)
Chin. Phys. B, 2025, 34 (**3**): 030203. DOI: 10.1088/1674-1056/ada54e

Darboux transformation, positon solution, and breather solution of the third-order flow Gerdjikov-Ivanov equation

Shuzhi Liu(刘树芝), Ning-Yi Li(李宁逸), Xiaona Dong(董晓娜), and Maohua Li(李茂华)
Chin. Phys. B, 2025, 34 (**1**): 010201. DOI: 10.1088/1674-1056/ad8ec6

A local refinement purely meshless scheme for time fractional nonlinear Schrödinger equation in irregular geometry region

Tao Jiang(蒋涛), Rong-Rong Jiang(蒋戎戎), Jin-Jing Huang(黄金晶), Jiu Ding(丁玖), and Jin-Lian Ren(任金莲)
Chin. Phys. B, 2021, 30 (**2**): 020202. DOI: 10.1088/1674-1056/abc0e0

Study and application of solitary wave propagation at fractional order of time based on SPH method

Luyang Ma(马璐阳), Rahmatjan Imin(热合买提江·依明)†, and Azhar Halik(艾孜海尔·哈力克)

College of Mathematics and Systems Science, Xinjiang University, Urumqi 830017, *China*

(Received 2 October 2024; revised manuscript received 31 December 2024; accepted manuscript online 6 March 2025)

A meshless particle method based on the smoothed particle hydrodynamics (SPH) method is first proposed for the numerical prediction of physical phenomena of nonlinear solitary wave propagation and complex phenomena arising from the inelastic interactions of solitary waves. The method is a fully discrete implicit scheme. This method does not rely on a grid, avoids the need to solve for derivatives of kernel functions, and makes the calculation more convenient. Additionally, the unique solvability of the proposed implicit scheme is proved. To verify the effectiveness and flexibility of the proposed method, we apply it to solving various time fractional nonlinear Schrödinger equations (TF-NLSE) on both regular and irregular domains. This mainly includes general or coupled TF-NLSE with or without analytical solutions. Moreover, the proposed method is compared with the existing methods. Through examples, it has been verified that this method can effectively predict complex propagation phenomena generated by the collision of nonlinear solitary waves, such as the collapse phenomenon of solitary waves with increasing fractional-order parameters. Research results indicate that this method provides a new and effective meshless method for predicting the propagation of nonlinear solitary waves, which can better simulate TF-NLSE in complex domains.

Keywords: Caputo fractional derivative, meshless particle method, nonlinear Schrödinger equation, irregular regions

PACS: 02.30.Jr, 02.60.–x, 02.70.–c, 02.70.Ns

DOI: 10.1088/1674-1056/adbd2a **CSTR:** 32038.14.CPB.adbd2a

1. Introduction

1.1. Overview of relevant work

In recent years, nonlinear science has become a research hotspot in the field of natural science, and nonlinear phenomena can be described by nonlinear differential equations. Nonlinear partial differential equations are widely used in fluid mechanics, quantum mechanics, physics, and other fields under the background of various disciplinary problems. Therefore, it is necessary to study nonlinear partial differential equations numerically. However, fractional calculus[1] can be used to describe and analyze some complex phenomena in the natural sciences. Compared with integer-order differential equations,[2–5] fractional partial differential equations[6–9] offer a closer approximation to the actual situation, when describing materials with memory and genetic properties. Therefore, the study of efficient numerical algorithms for fractional nonlinear partial differential equations has become an important research hotspot in scientific circles. After conducting a large number of studies, it has been found that the fractional nonlinear Schrödinger equation in fractional quantum mechanics[10–13] can describe most nonlinear physical phenomena. Such phenomena as Bose–Einstein condensates, plasma physics, nonlinear optics, nonlinear solitary wave diffusion,[3] and the interaction process of solitary wavelets, among others, are well described by fractional nonlinear partial differential equations. For example, it can describe the physical phenomena of modern optical soliton communication transmission and propagation of optical pulses in nonlinear media. Among them, solitons are also called solitary waves.

With the development of the times, fractional nonlinear Schrödinger equations and coupled fractional nonlinear Schrödinger systems influenced by fractional operators[14,15] have received widespread attention from researchers. In particular, the time fractional nonlinear Schrödinger equation describes the profile of a single soliton wave under fractional conditions and its propagation over time. To our knowledge, most numerical studies on the fractional Schrödinger equation are conducted in regular domains, while there is relatively few research on the fractional Schrödinger problem in irregular domains.[16] The coupled time fractional nonlinear Schrödinger equation is a two-component equation that models the formation and propagation of double isolated waves, as well as the inelastic collision process between two interacting solitary wavelets.[17,18] Due to the influence of the nonlinear term and fractional order, obtaining an analytical solution[19] for the fractional coupled Schrödinger equation is difficult. Therefore, various numerical simulation methods of fractional order have been widely used. Most of them are based on grid-based methods, such as the finite difference method,[20,21] the finite element method, the Galerkin method,[22] and the homotopy perturbation method.[23] Nonetheless, these grid-

†Corresponding author. E-mail: rahmatjanim@xju.edu.cn

© 2025 Chinese Physical Society and IOP Publishing Ltd. All rights, including for text and data mining, AI training, and similar technologies, are reserved.

based methods[24,25] can be complex and require significant computation when dealing with non-uniform distributions or irregular geometries. The coupled time fractional nonlinear Schrödinger system can simulate two interacting nonlinear wave packets in a discrete conservative system. This is distinct from the physical phenomena observed in integer order cases, such as the collapse of isolated waves[26–28] under the influence of fractional order. Although extensive research has been conducted on integer-order systems,[29,30] to our knowledge, there is relatively few research on fractional coupled systems. The time fractional Schrödinger equation is an extension of one of the most important and fundamental equations in quantum mechanics, and it can be used to describe many complex physical phenomena. This equation has been widely used in quantum mechanics, physics, and other scientific fields. Therefore, research on numerical methods for solving the time fractional nonlinear Schrödinger equation is necessary.

Currently, meshless methods have gradually attracted the attention of researchers and are widely used in various PDEs because they do not need to generate meshes, are easy to compute, and have a greater advantage in dealing with irregular regions or inhomogeneous distributions. Common meshless methods are conventional SPH, corrected SPH, modified SPH, moving least squares (MLS), radial basis function (RBF), finite pointset method (FPM), and so on. Zhou *et al.*[31] used operator splitting techniques to solve coupled nonlinear Schrödinger equations, and compared it with the PML method to verify the effectiveness of the method. Wei *et al.*[32] developed and analyze an implicit fully discrete local discontinuous Galerkin (LDG) finite element method for solving the time fractional coupled Schrödinger system. Hu *et al.*[33] presented a two-grid finite element method with $L1$ scheme for solving the two-dimensional (2D) time fractional nonlinear Schrödinger equation. The classical $L1$ scheme is considered in the time direction and the finite element method is used in the space direction. It is verified both theoretically and numerically that the accuracy is guaranteed even in extremely rough spaces. Jiang *et al.*[34] proposed a local refinement hybrid scheme to solve the 2D time fractional nonlinear Schrödinger equation in regularly or irregularly shaped domains, and extends the scheme to predict the quantum mechanical properties governed by the time fractional Gross–Pitaevskii equation with the rotating Bose–Einstein condensate. Abbaszadeh M *et al.*[35] introduced a new type of numerical solution based on Pascal's polynomials and multiscale ideas. The advantage of this technique is the construction of Pascal polynomials from monomials. The Pascal polynomials will be used to estimate the spatial derivatives of the SFPDEs on different non-rectangular physical regions. Heydari *et al.*[36] proposed an efficient moving least squares (MLS) meshfree approximation method to solve the nonlinear variable-order time fractional 2D Ginzburg–Landau equation by replacing the conventional derivative with the Atangana–Baleanu–Caputo fractional derivative. Okposo *et al.*[37] used an efficient novel technique, namely, the q-homotopy analysis transform method, to obtain analytical solutions for a system of time-fractional coupled nonlinear Schrödinger equations, with the time-fractional derivative taken in the Caputo sense. Jiang *et al.*[38] presented for the first time an accelerated novel meshless coupling algorithm for the numerical study of fractional-order nonlinear Schrödinger or Gross–Pitaevskii equations (SFNLS/GPE) in high dimensional spaces. Meanwhile, a parallel algorithm based on the above approximation scheme is designed to reduce the computational cost of GPU cards based on CUDA programs. Khayyer *et al.*[39] presented a new set of improvements to increase the accuracy and stability of the updated lagrangian SPH (ULSPH) used for structural modelling. Xu *et al.*[40] presented an SPH method for modelling transient viscoelastic fluid flows governed by the Phan Thien-Tanner (PTT) constitutive equation. A hybrid symmetry correction algorithm with kernel gradients is used to improve the computational accuracy of the SPH method. The tensile instability is eliminated by adding an artificial stress model to the momentum equation. In addition, the SPH solutions are compared with those obtained by the finite volume method (FVM) and the l2 paradigm errors of different SPH solutions to the FVM solutions are analyzed to verify the validity and advantages of the method. Hosseini *et al.*[41] considered the coupled nonlinear Schrödinger equations satisfying the Painlevé property, and as a result, they derived their solitary waves formally using a generalized method based on the technique of variable transformation. Li *et al.*[42] proposed coupled pure meshless finite pointset method to numerically predict the inelastic collision process of solitary waves described with the time fractional coupled nonlinear Schrödinger equation.

1.2. Major work in the present paper

Based on the above analysis, many meshless methods have been widely used to simulate various fluid/solid mechanics problems, but the modified SPH method adopted in this paper as a pure meshless particle method, which has not been applied to TF-NLSE, is mesh-independent and does not need to compute the kernel function derivatives. Compared with the conventional SPH, the modified SPH method used in this paper has higher accuracy and stability and is easier to implement than other meshless methods. In this section, our main work is presented. Firstly, a hybrid meshless particle method is introduced for numerically predicting nonlinear solitary wave propagation in fractional order of time. Specifically, our method utilizes the $L3$ approximate scheme[43] for the Caputo fractional derivative term and employs an improved SPH method[44] to discretize the spatial derivative term. Secondly, we extended the numerical method for solving the time frac-

tional Schrödinger equation and proved the solvability of the method presented in this paper. Meanwhile, compared to other existing numerical methods, the numerical results presented in this paper demonstrate smaller errors and better convergence speed. As far as we know, the method proposed in this paper has not been utilized to solve the time fractional Schrödinger equation.

The aim of this paper is to combine the $L3$ scheme with the improved SPH method, and apply it to study the physical phenomena of solitary wave propagation in both regular and irregular regions. The various sections of this paper are organized as follows. In Section 2, two forms of time fractional nonlinear Schrödinger equations and their initial and boundary conditions are presented. These equations can be used to describe the propagation phenomena of time fractional nonlinear solitary waves. In Section 3, the discrete scheme for the Caputo derivative of TF-NLSE and related lemmas are introduced in detail. In Section 4, an improved SPH method is described in detail. To avoid grid-based computations and enhance the reliability of numerical predictions for solitary wave propagation, we combine the $L3$ scheme with an improved SPH method for the first time and apply it to the fractional nonlinear Schrödinger equation. The derivation of the numerical scheme and an overview of the specific algorithmic steps are given in Section 5. Additionally, the theorem related to the implicit format presented in this paper and its proof are also given. Numerical experiments on nonlinear solitary waves with the same and different initial values, in regular and irregular regions are studied in Section 6. The phenomena generated by the inelastic collision process of solitary waves in fractional-order were predicted through numerical experiments. It is also verified that the proposed method can achieve high numerical accuracy when dealing with the coupled time fractional Schrödinger equation. In this section, the numerical simulation results obtained by the method in this paper are compared with the analytical solution and other results in the literature. Section 7 provides conclusions and prospects for the future. This study enhances our understanding of the propagation mechanism of time fractional nonlinear solitary waves and illuminates some of the strange and complex phenomena associated with their propagation.

2. Time fractional nonlinear Schrödinger equation

The propagation process of nonlinear solitary wave can be described by fractional nonlinear Schrödinger equation. This equation is a fundamental dynamic equation, and it can express many mathematical models of physical problems. The time fractional nonlinear Schrödinger equation describes the profile and propagation of fractional solitary wave over time. The soliton height refers to the highest peak, the soliton width is the overall width, and the peak distance is the separation distance. The coupled time fractional nonlinear Schrödinger equation is a two-component nonlinear fractional Schrödinger equation. It can describe the formation and propagation of double solitary waves, as well as the inelastic collision process between two interacting solitary wave. The following two forms of time fractional nonlinear Schrödinger equations were studied.

(i) Time fractional nonlinear Schrödinger equation[13]

$$\begin{cases} \mathrm{i}\,{}_0^C D_t^\alpha u(\boldsymbol{x},t)+\beta\Delta u+V(\boldsymbol{x})u \\ +\lambda g(|u(\boldsymbol{x},t)|^2)u=f(\boldsymbol{x},t), \\ u(\boldsymbol{x},0)=u_0(\boldsymbol{x}),\ \ \boldsymbol{x}\in\Omega, \\ u(\boldsymbol{x},t)=m(\boldsymbol{x},t),\ \ \boldsymbol{x}\in\partial\Omega,\ \ t\in[0,T], \end{cases} \tag{1}$$

where $u(\boldsymbol{x},t)$ is the complex valued wave function, $\mathrm{i}=\sqrt{-1}$ represents the imaginary part unit, β is a real value, Δ is the d-dimensional Laplace operator $(d=1,2)$, Ω is the simulated smooth region, λ is the coefficient describing the interaction strength of the nonlinear term $g(|u|^2)u$, is a real constant, T is a positive real constant. $V(\boldsymbol{x})$ is a real valued potential function, where the spatial variable $\boldsymbol{x}=(x,y)$. $\partial^\alpha u(\boldsymbol{x},t)/\partial t^\alpha$ is the Caputo fractional differential operator of $0<\alpha<1$, the time fractional Caputo derivative of $0<\alpha<1$ is defined as

$${}_0^C D_t^\alpha u(\boldsymbol{x},t)=\frac{1}{\Gamma(1-\alpha)}\int_0^t (t-s)^{(-\alpha)}\frac{\partial u(\boldsymbol{x},s)}{\partial s}\,\mathrm{d}s, \tag{2}$$

where $\Gamma(\cdot)$ represents the usual gamma function.

(ii) Coupled time fractional nonlinear Schrödinger equation

$$\begin{cases} \mathrm{i}\,{}_0^C D_t^\alpha u(x,t)+\sigma\Delta u+\lambda_1 u+\lambda_2 v+\eta(|u|^2+\rho|v|^2)u=f_1, \\ \mathrm{i}\,{}_0^C D_t^\alpha v(x,t)+\sigma\Delta v+\mu_1 u-\mu_2 v+\eta(\rho|u|^2+|v|^2)v=f_2. \end{cases} \tag{3}$$

The initial value condition of the above equation is

$$u(\boldsymbol{x},0)=u_0(\boldsymbol{x}),\quad x\in\Omega. \tag{4}$$

The boundary conditions are typically either periodic boundary conditions or Dirichlet boundary conditions. Where $\mathrm{i}^2=-1$ is an imaginary unit, parameter $0<\alpha<1$ is the amplitude of u, v complex valued wave or the envelope of two wave packets, $\sigma>0$ represents the group velocity dispersion, η can describe the nonlinear interaction strength, ρ stands for cross-phase modulation, function f_1 and f_2 are the source term of the equation, where $\partial\Omega$ refers to the boundary of the domain Ω.

3. Discrete method of time fractional derivative

In recent years, several discrete schemes have been proposed and widely used to approximate the Caputo fractional derivative in solving fractional differential equations. Among them, the $L1$ formula[48] with $o(\tau^{2-\alpha})$-order and $L1-2$ formula[49] with $o(\tau^{3-\alpha})$-order are more commonly used. This article uses the $L3$ formula,[43] which has been proposed

for a shorter period of time. This section proves the solvability of the $L3$ scheme, and gives its related lemmas and theorems. Here, Let M and N be positive integers, set time step to $\tau = T/M$, space step to $\Delta x = L/N$. Then use $0 \le i \le N-1$ to define space node $x_i = \mathrm{i}\Delta x$, and use $0 \le j \le M-1$ to define time node $t_j = j\tau$, $t_{j+1/2} = (t_j + t_{j+1})/2$. Therefore, the corresponding $L3$ difference method for the Caputo fractional derivative is as follows:[43]

$$ {}_0^C\mathbb{D}_t^{(\alpha)} u^k \approx \frac{\tau^{-\alpha}}{\Gamma(2-\alpha)} \left[\omega_0^{(\alpha)} u^k - \sum_{j=1}^{k-1} \left(\omega_{k-j-1}^{(\alpha)} - \omega_{k-j}^{(\alpha)} \right) u^j - \omega_{k-1}^{(\alpha)} u^0 \right], \tag{5} $$

where $0 \le j \le k-1$. When $k=1$, $\omega_0^{(\alpha)} = 1$; $k=2$, $\omega_0^{(\alpha)} = a_0^{(\alpha)} + b_0^{(\alpha)}$, $\omega_1^{(\alpha)} = a_1^{(\alpha)} - b_0^{(\alpha)}$; $k=3$,

$$ \omega_j^{(\alpha)} = \begin{cases} a_j^{(\alpha)} + b_j^{(\alpha)} + \gamma_j^{(\alpha)}, & j=0, \\ a_j^{(\alpha)} + b_j^{(\alpha)} - b_{j-1}^{(\alpha)} - 2\gamma_j^{(\alpha)}, & j=1, \\ a_j^{(\alpha)} - b_{j-1}^{(\alpha)} + \gamma_{j-2}^{(\alpha)}, & j=2, \end{cases} \tag{6} $$

for $k \ge 4$,

$$ \omega_j^{(\alpha)} = \begin{cases} a_j^{(\alpha)} + b_j^{(\alpha)} + \gamma_j^{(\alpha)}, & j=0, \\ a_j^{(\alpha)} + b_j^{(\alpha)} - b_{j-1}^{(\alpha)} + \gamma_j^{(\alpha)} - 2\gamma_{j-1}^{(\alpha)}, & j=1, \\ a_j^{(\alpha)} + b_j^{(\alpha)} - b_{j-1}^{(\alpha)} + \gamma_j^{(\alpha)} - 2\gamma_{j-1}^{(\alpha)} + \gamma_{j-2}^{(\alpha)}, & 2 \le j \le k-3, \\ a_j^{(\alpha)} + b_j^{(\alpha)} - b_{j-1}^{(\alpha)} - 2\gamma_{j-1}^{(\alpha)} + \gamma_{j-2}^{(\alpha)}, & j=k-2, \\ a_j^{(\alpha)} - b_{j-1}^{(\alpha)} + \gamma_{j-2}^{(\alpha)}, & j=k-1, \end{cases} \tag{7} $$

with $a_j^{(\alpha)} = (j+1)^{1-\alpha} - j^{1-\alpha}$, $0 \le j \le k-1$; $b_j^{(\alpha)} = [(j+1)^{2-\alpha} - j^{2-\alpha}]/(2-\alpha) - [(j+1)^{1-\alpha} + j^{1-\alpha}]/2$, $j \ge 0$;

$$ \beta_j^{(\alpha)} = -\left(\frac{1}{6}((j+1)^{1-\alpha} + 2j^{1-\alpha}) + \frac{1}{2-\alpha} j^{2-\alpha} - \frac{1}{(2-\alpha)(3-\alpha)}((j+1)^{3-\alpha} - j^{3-\alpha}) \right), \quad j \ge 0. $$

Here, for $k=2$, $\omega_0^{(\alpha)} \in (1, 3/2)$; For $k \ge 3$, $\omega_0^{(\alpha)} \in (1, 11/6)$. The properties of the coefficients a_j, b_j, c_j, ω_j can be found in Ref. [43].

Lemma 1 For any α $(0 < \alpha < 1)$, and $\omega_j^{(\alpha)}$ $(2 \le j \le k-1, k \ge 4)$ is defined by Eqs. (6) and (7), we have (i) $\omega_0^{(\alpha)} \ge |\omega_1^{(\alpha)}|$; (ii) $\omega_j^{(\alpha)} > 0$, $j \ne 1$; (iii) $\omega_2^{(\alpha)} \ge \omega_3^{(\alpha)} \ge \cdots \ge \omega_{k-1}^{(\alpha)}$; (iv) $\omega_0^{(\alpha)} \ge \omega_2^{(\alpha)}$; (v) $\Sigma_{j=0}^{k-1} \omega_0^{(\alpha)} = k^{(1-\alpha)}$.

Proof See Ref. [43].

Lemma 2 Assuming $f \in C^4[0, t_k]$. For any α, ${}_0^C\mathbb{D}_t^{(\alpha)} u(t)|_{t=t_k}$ is defined as shown in Eq. (5). Here $|R(u(t_k))| = {}_0^C D_t^{(\alpha)} u(t)|_{t=t_k} - {}_0^C \mathbb{D}_t^{(\alpha)} u(t)|_{t=t_k}$. We have

$$ \begin{aligned} &|R(f(t_1))| \\ &\le \frac{\alpha}{2\Gamma(3-\alpha)} \Delta t^{2-\alpha} \max_{t_0 \le t \le t_1} f''(t), \\ &|R(f(t_2))| \\ &\le \frac{\alpha}{\Gamma(1-\alpha)} \left(\frac{1}{12} \max_{t_0 \le t \le t_1} |f''(t)| (t_2 - t_1)^{-\alpha-1} \Delta t^3 \right. \\ &\quad \left. + \frac{1}{3(1-\alpha)(2-\alpha)} \left(\frac{1}{2} + \frac{1}{3-\alpha} \right) \max_{t_0 \le t \le t_2} |f'''(t)| \Delta t^{3-\alpha} \right), \\ &|R(f(t_k))| \\ &\le \frac{\alpha}{\Gamma(1-\alpha)} \left(12(t_k - t_1)^{-\alpha-1} \max_{t_0 \le t \le t_1} |f''(t)| \Delta t^3 \right. \\ &\quad + \frac{1}{8}(t_k - t_2)^{-\alpha-1} \max_{t_0 \le t \le t_2} |f'''(t)| \Delta t^4 \\ &\quad \left. + \left(\frac{1}{2} + \frac{1}{12} \frac{27 - 10\alpha + \alpha^2}{\prod_{i=1}^4 (\alpha - i)} \right) \max_{t_0 \le t \le t_k} |f^{(4)}(t)| \Delta t^{4-\alpha} \right), \end{aligned} $$

$$ k \ge 3. \tag{8} $$

Proof See Ref. [43].

Lemma 3 The following difference scheme (Eq. (10)) is uniquely solvable. Consider the following time fractional Schrödinger problem

$$ \begin{cases} \mathrm{i}\, {}_0^C D_t^{\alpha} u(x,t) = u_{xx}(x,t) + f(x,t), \\ u(x,0) = u_0(x), \\ u(0,t) = m(t), u(L,t) = n(t), \quad x \in [0, L], \end{cases} \tag{9} $$

where $\alpha \in (0,1)$, f, m, u_0 are known functions. The following difference scheme is established:

$$ \begin{cases} \mathrm{i}\, \frac{\tau^{-\alpha}}{\Gamma(2-\alpha)} [\omega_0^{(\alpha)} u_i^k - \sum_{j=1}^{k-1} \left(\omega_{k-j-1}^{(\alpha)} - \omega_{k-j}^{(\alpha)} \right) u_i^j - \omega_{k-1}^{(\alpha)} u_i^0] \\ = \delta_x^2 u_i^k + f_i^k, \\ u_i^0 = u_0(x_i), \quad 1 \le i \le M-1, \\ u_0^k = m(t_k), u_M^k = n(t_k), \quad 0 \le k \le N, \end{cases} \tag{10} $$

where the time fractional derivative is approximated by the $L3$ scheme, and the space derivative is discretized by the second-order central difference quotient. Similar proof can be found in Ref. [48].

Proof Here notate $u^k = (u_0^k, u_1^k, \ldots, u_M^k)$, and since u^0 is known, and $u^1, u^2, \ldots, u^{k-1}$ are uniquely determined, a linear equation on u^k can be obtained from Eq. (10). To prove its unique solvability, it is necessary to show that the following

equation has only zero solutions:

$$\begin{cases} \mathrm{i}\,\dfrac{1}{\tau^{\alpha}\Gamma(2-\alpha)}u_i^k=\delta_x^2 u_i^k, \\ u_0^k=u_M^k=0. \end{cases} \tag{11}$$

Suppose $\|u\|_\infty=|u_{i_k}^k|, i_k\in 1,2,\ldots,M-2$. Equation (11) can be rewritten as

$$(1-2\mathrm{i}\mu)u_i^k=-\mathrm{i}\mu u_{i-1}^k-\mathrm{i}\mu u_{i+1}^k. \tag{12}$$

Let $i=i_k$ and take modulo $|\cdot|$ on both sides of the equation, and use trigonometric inequalities and boundary conditions to obtain

$$\sqrt{(1+4\mu^2)}\|u^k\|_\infty\le 2\mu\|u^k\|_\infty, \tag{13}$$

so $\|u^k\|_\infty=0$, where $\mu=\frac{\tau^\alpha\Gamma(2-\alpha)}{h^2}$. We can easily get $u^k=0$.

Lemma 4 Let us assume that the solution of Eq. (14) is an analytic function on the interval $\Omega\times[0,T]$, where u^k belongs to $L^2(\Omega)$. Then, the scheme defined by Eq. (15) is unconditionally stable in $L^2(\Omega)$. Therefore we study the unique solvability of the time discretization scheme given in Eq. (15)

$$\begin{cases} \mathrm{i}\,{}_0^C D_t^\alpha u(\boldsymbol{x},t)+\beta\Delta u+V(\boldsymbol{x})u=f(\boldsymbol{x},t), \\ u(\boldsymbol{x},0)=u_0(\boldsymbol{x}),\quad \boldsymbol{x}\in\Omega, \\ u(\boldsymbol{x},t)=m(\boldsymbol{x},t),\quad \boldsymbol{x}\in\partial\Omega, t\in[0,T]. \end{cases} \tag{14}$$

The corresponding semi-discrete format is as follows:

$$\begin{aligned} &\omega_0^{(\alpha)}u^k-\mathrm{i}r[\beta\Delta u^k+Vu^k] \\ &=-\mathrm{i}rf^k+\sum_{j=1}^{N}(\omega_{k-j-1}^{(\alpha)}-\omega_{k-j}^{(\alpha)})u^j+\omega_{k-1}^{(\alpha)}u^0, \end{aligned} \tag{15}$$

with $r=\tau^\alpha\Gamma(2-\alpha)$.

Proof The error e^k at the n-th level is denoted as $e^k=u^k-U^k$. Here, u^k and U^k are analytical solution and numerical solution, respectively.

$$\begin{aligned} &\omega_0^{(\alpha)}e^k-\mathrm{i}r[\beta\Delta e^k+Ve^k] \\ &=\sum_{j=1}^{N}(\omega_{k-j-1}^{(\alpha)}-\omega_{k-j}^{(\alpha)})e^j+\omega_{k-1}^{(\alpha)}e^0. \end{aligned} \tag{16}$$

Multiplying Eq. (16) by e^k and integrating it over the region Ω, we get

$$\begin{aligned} &\omega_0^{(\alpha)}\langle e^k,e^k\rangle-\mathrm{i}r\beta\langle\Delta e^k,e^k\rangle-\mathrm{i}r\langle Ve^k,e^k\rangle \\ &=\sum_{j=1}^{N}(\omega_{k-j-1}^{(\alpha)}-\omega_{k-j}^{(\alpha)})\langle e^j,e^k\rangle+\omega_{k-1}^{(\alpha)}\langle e^0,e^k\rangle. \end{aligned} \tag{17}$$

Using $e^k\in L_0^2(\Omega)$ and Green's formula, we have

$$\begin{aligned} &\omega_0^{(\alpha)}\|e^k\|_{L^2(\Omega)}^2-\mathrm{i}r\beta\|\nabla e^k\|_{L^2(\Omega)}^2-\mathrm{i}r\langle Ve^k,e^k\rangle \\ &=\sum_{j=1}^{N}(\omega_{k-j-1}^{(\alpha)}-\omega_{k-j}^{(\alpha)})\langle e^j,e^k\rangle+\omega_{k-1}^{(\alpha)}\langle e^0,e^k\rangle. \end{aligned} \tag{18}$$

Here, $L_0^2(\Omega)\in\{u\in L^2(\Omega):u\,|_{\partial\Omega=0}\}$. In the above expression, based on the definition of the inner product, we can conclude that $V(x)\langle e^k,e^k\rangle$ is a real value. Next, we take the absolute value of both sides of Eq. (18), using the definitions of complex numbers and triangle inequality. Next, using the Schwarz inequality, we can obtain

$$\begin{aligned} \omega_0^{(\alpha)}\|e^k\|_{L^2(\Omega)}^2 &\le \sum_{j=1}^{N}(\omega_{k-j-1}^{(\alpha)}-\omega_{k-j}^{(\alpha)})\|e^j\|_{L^2(\Omega)}\|e^k\|_{L^2(\Omega)} \\ &\quad+\omega_{k-1}^{(\alpha)}\|e^0\|_{L^2(\Omega)}\|e^k\|_{L^2(\Omega)} \\ &=\left[\sum_{j=1}^{N}(\omega_{k-j-1}^{(\alpha)}-\omega_{k-j}^{(\alpha)})\|e^j\|_{L^2(\Omega)}\right. \\ &\quad\left.+\omega_{k-1}^{(\alpha)}\|e^0\|_{L^2(\Omega)}\right]\|e^k\|_{L^2(\Omega)}. \end{aligned} \tag{19}$$

Here, when $k=1$, we have $\|e^1\|_{L^2(\Omega)}\le\|e^0\|_{L^2(\Omega)}$. By mathematical induction, we assume that the following equation also holds:

$$\|\,e^j\,\|_{L^2(\Omega)}\le\|e^0\|_{L^2(\Omega)},\quad j=1,2,\ldots,k-1. \tag{20}$$

Next, we only need to prove the following equation:

$$\|\,e^k\,\|_{L^2(\Omega)}\le\|e^0\|_{L^2(\Omega)}. \tag{21}$$

By Eqs. (19) and (20), we have

$$\begin{aligned} &\omega_0^{(\alpha)}\|e^k\|_{L^2(\Omega)}^2 \\ &\le\left[\sum_{j=1}^{N}(\omega_{k-j-1}^{(\alpha)}-\omega_{k-j}^{(\alpha)})\|e^j\|_{L^2(\Omega)}\right. \\ &\quad\left.+\omega_{k-1}^{(\alpha)}\|e^0\|_{L^2(\Omega)}\right]\|e^k\|_{L^2(\Omega)} \\ &\le\left[\sum_{j=1}^{N}(\omega_{k-j-1}^{(\alpha)}-\omega_{k-j}^{(\alpha)})+\omega_{k-1}^{(\alpha)}\right]\|e^0\|_{L^2(\Omega)}, \end{aligned} \tag{22}$$

$$\begin{aligned} &\|e^k\|_{L^2(\Omega)}^2 \\ &=(\omega_0^{(\alpha)})^{-1}\left[\sum_{j=1}^{N}(\omega_{k-j-1}^{(\alpha)}-\omega_{k-j}^{(\alpha)})+\omega_{k-1}^{(\alpha)}\right]\|e^0\|_{L^2(\Omega)} \\ &\le\|e^0\|_{L^2(\Omega)}. \end{aligned} \tag{23}$$

From the principle of mathematical induction, Lemma 4 is valid.

4. Spatial derivative approximation

4.1. Traditional smoothed particle hydrodynamics method

The traditional SPH method[50] includes two main steps: kernel approximation and particle approximation. Each particle has its own volume, mass, and density. The integral expression of function $u(\boldsymbol{x})$ is as follows:[50]

$$u(\boldsymbol{x})=\int_{-\infty}^{+\infty}u(\boldsymbol{x}')\delta(\boldsymbol{x}-\boldsymbol{x}')\mathrm{d}\boldsymbol{x}', \tag{24}$$

where δ is the Dirac function.

The kernel approximation expression of the function u and its partial derivatives ∇u is as follows:[50]

$$\langle u(\boldsymbol{x})\rangle = \frac{1}{h^d}\int_\Omega u(\boldsymbol{x}')\,W\left(\frac{\boldsymbol{x}-\boldsymbol{x}'}{h}\right)\mathrm{d}\boldsymbol{x}'. \tag{25}$$

If the smoothing kernel function possesses a continuous spatial derivative of the corresponding order, then we can obtain the kernel approximation expression of the spatial derivative of any order as follows:[50]

$$\left\langle \frac{\partial^n u(\boldsymbol{x})}{\partial \boldsymbol{x}^n}\right\rangle = \frac{1}{h^d}\int_\Omega u(\boldsymbol{x}')\frac{\partial^n W(\frac{\boldsymbol{x}-\boldsymbol{x}'}{h})}{\partial \boldsymbol{x}^n}\mathrm{d}\boldsymbol{x}', \tag{26}$$

where d represents the dimension of the function, the symbol $\langle\cdot\rangle$ represents the kernel approximation expression, $\Omega: |\boldsymbol{x}-\boldsymbol{x}'|<\kappa h$ is the domain affected by the kernel function, κ is the constant dependent on the kernel function, and h is the smoothing length.

In the process of particle approximation, the calculation region is discretized into a series of particles for particle search. Particle volume is $\mathrm{d}x' = \Delta V = m/\rho$, ρ is particle density, and m is particle mass. Then the particle approximation expression is as follows:

$$\langle u(\boldsymbol{x})\rangle \approx \sum_{k=1}^{N}\frac{m_k}{\rho_k}u(\boldsymbol{x}_k)\,W(\boldsymbol{x}-\boldsymbol{x}_k,h), \tag{27}$$

$$\left\langle \frac{\partial^n u(\boldsymbol{x})}{\partial \boldsymbol{x}^n}\right\rangle \approx \sum_{k=1}^{N}\frac{m_k}{\rho_k}u(\boldsymbol{x}_k)\frac{\partial^n}{\partial \boldsymbol{x}^n}W(\boldsymbol{x}-\boldsymbol{x}_k,h), \tag{28}$$

where N is the total number of discrete particles in the influence region, h is the smoothing length, and $\boldsymbol{x}_k$ represents the neighboring particles of the particle at $\boldsymbol{x}$. The error in the process of particle approximation is related to the choice of kernel function W, particle spacing $\Delta\boldsymbol{x}$ and kernel smoothing length h. In addition, the symbol $\langle\cdot\rangle$ in the above equation stands for the smooth kernel function approximation operator.

4.2. An improved smoothed particle hydrodynamics method

The Taylor series expansion of function u at $\boldsymbol{x}'$, as shown below:

$$\begin{aligned} u(\boldsymbol{x}') &= u(\boldsymbol{x}) + \sum_{\alpha=1}^{d}(x'_\alpha - x_\alpha)u'_{\boldsymbol{x}'_\alpha}(\boldsymbol{x}) \\ &\quad + \sum_{\alpha,\beta=1}^{d}\frac{1}{2}(x'_\alpha - x_\alpha)(x'_\beta - x_\beta)u''_{\boldsymbol{x}'_\alpha\boldsymbol{x}'_\beta}(\boldsymbol{x}) + \cdots. \end{aligned} \tag{29}$$

Both sides of Eq. (29) are multiplied by W, $[(x'_k - x_k)/h]W$ and $[(x'_k - x_k)h]/[(x'_l - x_l)/h]W$, and then integrated over the influence domain of the kernel function. This leads to the corresponding particle approximation expressions as follows:

$$\begin{aligned} \langle u(\boldsymbol{x})\rangle &= M_0 u(\boldsymbol{x}) + h\sum_{\alpha=1}^{d}M_1^\alpha u'_{\boldsymbol{x}_\alpha} \\ &\quad + \frac{h^2}{2}\sum_{\alpha,\beta=1}^{d}M_2^{\alpha\beta}u''_{\boldsymbol{x}_\alpha\boldsymbol{x}_\beta} + o(h^3), \end{aligned} \tag{30}$$

$$\begin{aligned} &\left\langle \frac{x'_k - x_k}{h}u(\boldsymbol{x})\right\rangle \\ &= M_1^k u(\boldsymbol{x}) + h\sum_{\alpha=1}^{d}M_2^{\alpha k}u'_{\boldsymbol{x}_\alpha} \\ &\quad + \frac{h^2}{2}\sum_{\alpha,\beta=1}^{d}M_3^{\alpha\beta k}u''_{\boldsymbol{x}_\alpha\boldsymbol{x}_\beta} + o(h^3), \end{aligned} \tag{31}$$

$$\begin{aligned} &\left\langle \left(\frac{x'_k - x_k}{h}\frac{x'_l - x_l}{h}\right)u(\boldsymbol{x})\right\rangle \\ &= M_2^{kl}u(\boldsymbol{x}) + h\sum_{\alpha=1}^{d}M_3^{\alpha kl}u'_{\boldsymbol{x}_\alpha} \\ &\quad + \frac{h^2}{2}\sum_{\alpha,\beta=1}^{d}M_4^{\alpha\beta kl}u''_{\boldsymbol{x}_\alpha\boldsymbol{x}_\beta} + o(h^3), \end{aligned} \tag{32}$$

where

$$\begin{aligned} &M_n^{k_1k_2\cdots k_n} \\ &= \frac{1}{h^d}\int_\Omega \frac{x'_{k_1}-x_{k_1}}{h}\frac{x'_{k_2}-x_{k_2}}{h}\cdots\frac{x'_{k_n}-x_{k_n}}{h}W\left(\frac{x'-x}{h}\right)\mathrm{d}x', \end{aligned}$$

M_n is the n-order moment of the kernel function and is independent of the smooth length. α and β are related dummy marks for the number of function independent variables. Specially, the symbol $\langle\cdot\rangle$ in the above equation stands for the smooth kernel function approximation operator.

For the high-dimensional case, we can obtain the first-order derivative formula for the function $u(\boldsymbol{x})$

$$u'_{\boldsymbol{x}_\alpha}(\boldsymbol{x}) = \frac{\left\langle \frac{x'_k - x_k}{h}u(\boldsymbol{x})\right\rangle}{hM_2^{\alpha k}} + o(h^2). \tag{33}$$

For the second-order derivative formula, we get the following expressions:

$$u''_{\boldsymbol{x}_\alpha^2}(\boldsymbol{x}) = \frac{2}{h^2}\left[M_4^{\alpha\alpha kk}\right]^{-1}\left[\left\langle\left(\frac{x'_k - x_k}{h}\right)^2 u(\boldsymbol{x})\right\rangle - M_2^{kk}u(\boldsymbol{x})\right] + o(h^2), \tag{34}$$

$$\begin{pmatrix} u''_{x_1^2}(\boldsymbol{x}) \\ u''_{x_2^2}(\boldsymbol{x}) \\ \vdots \\ u''_{x_d^2}(\boldsymbol{x}) \end{pmatrix} = \left(\frac{h^2}{2}M_4^{\alpha\alpha kk}\right)^{-1}_{d\times d}\begin{pmatrix} \langle(\frac{x'_1-x_1}{h})^2u(\boldsymbol{x})\rangle - M_2^{x_1x_1}u(\boldsymbol{x}) \\ \langle(\frac{x'_2-x_2}{h})^2u(\boldsymbol{x})\rangle - M_2^{x_2x_2}u(\boldsymbol{x}) \\ \vdots \\ \langle(\frac{x'_d-x_d}{h})^2u(\boldsymbol{x})\rangle - M_2^{x_dx_d}u(\boldsymbol{x}) \end{pmatrix} + o(h^2). \tag{35}$$

Here, d represents the dimension of the function u. This method's calculation process does not necessitate the derivative of the kernel function, thus reducing the requirements for the kernel function. Consequently, the optional kernel function range is wider and the calculation speed is accelerated. We use the improved SPH method[44] in this section to numerically study the propagation of fractional order solitary waves. In addition, the selection of smooth kernel function W is crucial for numerical accuracy and stability. To facilitate this, we use the following kernel function.

Double-cosine kernel function[45]

$$W(x-x',h) = \frac{\alpha}{(kh)^d}\begin{cases} 4\cos\left(\frac{\pi}{k}s\right)+\cos\left(\frac{2\pi}{k}s\right)+3, & 0\le s<k,\\ 0, & s\ge k. \end{cases} \tag{36}$$

In the one-dimensional (1D), two-dimensional (2D), and three-dimensional (3D) cases, α takes the value of $1/6$, $\pi/(3\pi^2-16)$, and $\pi/(4\pi^2-30)$, respectively. The constant k is used to adjust the non-negative region. In particular, $r=|x-x'|$, $s=r/h$, r stands for the distance between points x and x'.

5. Numerical implementation

The initial value-boundary problem for the time fractional Schrödinger equation with Dirichlet or periodic boundary conditions is studied in this paper. For the boundary, we directly use the Dirichlet boundary conditions. By applying the given boundary values to the boundary particle sets in both regular and irregular regions, a fully discrete implicit scheme is further obtained.

In order to predict the propagation of solitary waves, a combined method is proposed in this paper, which utilizes FDM to approximate Caputo time fractional derivatives and employs an improved SPH method to discretize spatial derivatives. This meshless method avoids solving the derivative of kernel function and requires less computation. Specifically, the discrete region Ω_i, Therefore, the discrete format of TF-NLSE can be written as

$$\begin{cases} \mathrm{i}\,{}_0^C D_t^\alpha u(\boldsymbol{x},t_k)+\beta\Delta u(\boldsymbol{x},t_k)+V(\boldsymbol{x})u(\boldsymbol{x},t_k)\\ +\lambda g(|u(\boldsymbol{x},t_{k-1})|^2)u(\boldsymbol{x},t_k)=f(\boldsymbol{x},t_k),\\ u(\boldsymbol{x},0)=u_0(\boldsymbol{x}),\\ u(\boldsymbol{x},t_k)=m(\boldsymbol{x},t_k). \end{cases} \tag{37}$$

The $L3$ approximation at t_k is used to approximate the time fractional derivative defined in the Caputo sense, and the spatial derivative discretisation has been carried out using the improved SPH method. Therefore, the implicit scheme used in this paper is specifically derived as follows:

$$\begin{aligned} &\mathrm{i}\,{}_0^C D_t^\alpha u(\boldsymbol{x},t_k)\\ &=-\varepsilon[\beta\Delta u(\boldsymbol{x},t_k)+V(\boldsymbol{x})u(\boldsymbol{x},t_k)\\ &\quad+\lambda g(|u(\boldsymbol{x},t_{k-1})|^2)u(\boldsymbol{x},t_k)]\\ &\quad-(1-\varepsilon)[\beta\Delta u(\boldsymbol{x},t_{k-1})+V(\boldsymbol{x})u(\boldsymbol{x},t_{k-1})\\ &\quad+\lambda g(|u(\boldsymbol{x},t_{k-2})|^2)u(\boldsymbol{x},t_{k-1})]+f(\boldsymbol{x},t_k). \end{aligned} \tag{38}$$

This article uses the well-known implicit scheme when $\varepsilon=1$,

$$\begin{aligned} &\mathrm{i}\,{}_0^C D_t^\alpha u(\boldsymbol{x},t_k)\\ &=-[\beta\Delta u(\boldsymbol{x},t_k)+V(\boldsymbol{x})u(\boldsymbol{x},t_k)\\ &\quad+\lambda g(|u(\boldsymbol{x},t_{k-1})|^2)u(\boldsymbol{x},t_k)]+f(\boldsymbol{x},t_k). \end{aligned} \tag{39}$$

The implicit discrete scheme employed in this paper can be summarized as follows:

$$\begin{aligned} &\mathrm{i}\eta[\omega_0^{(\alpha)}u^k-\sum_{j=1}^{k-1}(\omega_{k-j-1}^{(\alpha)}-\omega_{k-j}^{(\alpha)})u^j-\omega_{k-1}^{(\alpha)}u^0]\\ &=-[\beta(\Delta u^k)^{\text{improved SPH}}+V(\boldsymbol{x})u^k\\ &\quad+\lambda g(|u^{k-1}|^2)u^k]+f^k, \end{aligned} \tag{40}$$

$$\begin{aligned} &\mathrm{i}\eta\left[\omega_0^{(\alpha)}u_l^k-\sum_{j=1}^{k-1}(\omega_{k-j-1}^{(\alpha)}-\omega_{k-j}^{(\alpha)})u_l^j-\omega_{k-1}^{(\alpha)}u_l^0\right]\\ &=-\Bigg[2\beta\frac{\sum_{l=1}^{N-2}(\frac{m_j}{\rho_j}(\frac{x_j-x_l}{h})^2W_{lj}(u_j^k-u_l^k))}{h^2M_4}\\ &\quad+Vu_l^k+\lambda g(|u_l^{k-1}|^2)u_l^k\Bigg]-\beta\left[\frac{m_0}{\rho_0}\left(\frac{x_0-x_l}{h}\right)^2W_{0j}u_0^k\right.\\ &\quad\left.+\frac{m_{N-1}}{\rho_{N-1}}\left(\frac{x_{N-1}-x_l}{h}\right)^2W_{N-1,j}u_{N-1}^k\right]+f_l^k. \end{aligned} \tag{41}$$

Based on the above Eq. (41), we can obtain the following formula:

$$A^lM^k=N_l^k, \tag{42}$$

where

$$\begin{aligned} &A_{11}=a+\sum_{j=2}^{N-2}\Psi_{1j}+\mu_1,\\ &A_{jj}=a+\sum_{j=1}^{N-2}\Psi_{lj}-\Psi_{jj}+\mu_j,\\ &1\le j\le N-2,\ 2\le l\le N-2;\quad A_{lj}=-\Psi_{lj},\quad j\ne l.\\ &M=(u_1^k,u_2^k,\ldots,u_{N-2}^k),\\ &N_l=(b_1+f_1^k,b_2+f_2^k,\ldots,b_{N-2}+f_{N-2}^k),\\ &u^k=u(\boldsymbol{x},t_k),\quad \eta=\frac{1}{\tau^\alpha\Gamma(2-\alpha)},\\ &a=\mathrm{i}\eta\omega_0^{(k,\alpha)},\quad \mu_l=V_l+\lambda g(|u_l^{k-1}|^2),\\ &b_l=\mathrm{i}\left[\sum_{j=1}^{k-1}(\omega_{k-j-1}^{(\alpha)}-\omega_{k-j}^{(\alpha)})u_l^j+\omega_{k-1}^{(\alpha)}u_l^0\right]\\ &\quad-\beta\left[\frac{m_0}{\rho_0}\left(\frac{x_0-x_l}{h}\right)^2W_{0j}u_0^k\right.\\ &\quad\left.+\frac{m_{N-1}}{\rho_{N-1}}\left(\frac{x_{N-1}-x_l}{h}\right)^2W_{N-1,j}u_{N-1}^k\right], \end{aligned}$$

$$\Psi_{lj}=\frac{2\beta\frac{m_j}{\rho_j}\left(\frac{x_j-x_l}{h}\right)^2 W_{lj}}{M_4h^2}.$$

The 1D numerical discretization scheme is described above, and similarly, a high-dimensional discretization scheme can be derived.

Theorem 1 The implicit format Eq. (42) is uniquely solvable.

Proof Here, matrix A is transformed as follows:

$$A = B+\mathrm{i}C, \tag{43}$$

$$\begin{aligned} A^l &= \begin{pmatrix} \mathrm{i}\eta\omega_0^{(k,\alpha)}+\sum_{j=2}^{N-2}\Phi_{1j} & -\Phi_{12} & \cdots & -\Phi_{1,N-2} \\ -\Phi_{21} & \mathrm{i}\eta\omega_0^{(k,\alpha)}+\sum_{j=1}^{N-2}\Phi_{2j}-\Phi_{22} & \cdots & -\Phi_{2,N-2} \\ \vdots & \vdots & \vdots & \vdots \\ -\Phi_{N-2,1} & -\Phi_{N-2,2} & \cdots & \mathrm{i}\eta\omega_0^{(k,\alpha)}+\sum_{j=1}^{N-3}\Phi_{N-2,j} \end{pmatrix} \\ &= \begin{pmatrix} \sum_{j=2}^{N-2}\Phi_{1l} & -\Phi_{12} & \cdots & -\Phi_{1,N-2} \\ -\Phi_{21} & \sum_{j=1}^{N-2}\Phi_{2j}-\Phi_{22} & \cdots & -\Phi_{2,N-2} \\ \vdots & \vdots & \vdots & \vdots \\ -\Phi_{N-2,1} & -\Phi_{N-2,2} & \cdots & \sum_{j=1}^{N-3}\Phi_{N-2,j} \end{pmatrix} + \begin{pmatrix} \mathrm{i}\eta\omega_0^{(k,\alpha)} & & & \\ & \mathrm{i}\eta\omega_0^{(k,\alpha)} & & \\ & & \ddots & \\ & & & \mathrm{i}\eta\omega_0^{(k,\alpha)} \end{pmatrix} \\ &= B^l+\mathrm{i}C^l, \end{aligned} \tag{44}$$

where A^l, B^l, C^l are the matrix related to l.

$$\Phi_{lj}=\frac{2\frac{m_j}{\rho_j}\left(\frac{x_j-x_l}{h}\right)^2 W_{lj}}{M_4h^2}.$$

In order to obtain the unique solvability of the implicit scheme, we need to prove that the determinants of B and C mentioned above are not 0. Two sets of column vectors are given as follows:

$$B^1,B^2,\ldots,B^{N-2};\quad C^1,C^2,\ldots,C^{N-2}.$$

According to Lemma 1, it can be inferred that $\omega_0^{(k,\alpha)}>0$. Given that $\eta>0$, and matrix C is a diagonal matrix, $|C|>0$ is always holds. Assuming that the determinant of B is 0, the column vector group B is linearly correlated. Therefore, there are numbers that are not all zeros such that

$$\begin{aligned} &x_1B^1+X_2B^2+\cdots+X_{N-2}B^{N-2}=0, \\ &x_1\left(\sum_{j=2}^{N-2}\Phi_{1j},-\Phi_{21},-\Phi_{31},\cdots,-\Phi_{N-2,1}\right) \\ &+x_2\left(-\Phi_{12},\sum_{j=1}^{N-2}\Phi_{2j}-\Phi_{22},\cdots,-\Phi_{N-2,2}\right)+\cdots \\ &+x_{N-2}(-\Phi_{1,N-2},-\Phi_{2,N-2},\cdots, \\ &\sum_{j=1}^{N-2}\Phi_{N-2,j}-\Phi_{N-2,N-2})=0. \end{aligned} \tag{45}$$

We make $|x_j|>|x_l|$, and for $l=1$,

$$\begin{aligned} &x_1\left(\sum_{j=2}^{N-2}\Phi_{1j}\right)+x_2(-\Phi_{12})+\cdots+x_{N-2}(-\Phi_{1,N-2})=0, \\ &\sum_{j=2}^{N-2}\Phi_{1j}(x_l-x_j)=0. \end{aligned} \tag{47}$$

It is easy to see that $\Phi_{lj}>0$. If $x_1>0$, then $\sum_{j=2}^{N-2}\Phi_{1l}(x_j-x_l)>0$; If $x_1<0$, then $\sum_{j=2}^{N-2}\Phi_{1l}(x_j-x_l)<0$; Therefore, this contradicts Eq. (47) and the assumption does not hold. Let us put it another way, $|B|\neq 0$.

For $2\le l<N-2$,

$$\begin{aligned} &x_1(-\Phi_{lj})+x_2(-\Phi_{l2})+\cdots \\ &+x_l\left(\sum_{j=1}^{N-2}\Phi_{lj}-\Phi_{ll}\right)+\cdots+x_{N-2}(-\Phi_{l,N-2})=0, \\ &\sum_{j=1}^{l}\Phi_{lj}(x_j-x_l)-\Phi_{ll}=0. \end{aligned} \tag{48}$$

For $l=N-2$,

$$\sum_{j=1}^{N-2}\Phi_{lj}(x_j-x_l)-\Phi_{N-2,N-2}=0. \tag{49}$$

Similarly, it can be proven that $|B|\neq 0$. For any j, $|B|\neq 0$, $|C|\neq 0$, we can obtain $|A|\neq 0$, which means that the implicit format given in this paper is uniquely solvable.

Algorithm 1 Computing the numerical solution of TF-NLSE (Eq. (1)) ($0<\alpha<1$).

Input: Regular or irregular field Ω_i, source term f, initial condition and boundary condition.

Output: The discrete solution of the numerical solution of TF-NLSE on random node (x_i,t_k) is obtained by this scheme. To achieve this, follow these steps:

Step 1: Regional division.

Step 2: Apply the $L3$ scheme to the temporal fractional derivative, and discretize the spatial derivative using the improved SPH method.

Step 3: Use the initial condition to determine U_i^0, and the boundary condition to determine U_0^k and U_M^k. To obtain the numerical solution of the first time layer U_i^1.

Step 4: Apply the format provided in this article

$$\begin{aligned}&\eta[\omega_0^{(\alpha)}u^1-\omega_0^{(\alpha)}u^0]=\mathrm{i}[\beta(\Delta u^1)^{\text{improved SPH}}\\&+V(\boldsymbol{x})u^1+\lambda g(|u^0|^2)u^1]-if^1,\end{aligned}\tag{50}$$

$$\begin{aligned}&\eta\omega_0^{(\alpha)}u_l^1-\mathrm{i}[2\beta\frac{\sum_{l=1}^{N-2}(\frac{m_j}{\rho_j}(\frac{x_j-x_l}{h})^2W_{lj}(u_j^1-u_l^1))}{h^2M_4}\\&+Vu_l^1+\lambda g(|u_l^0|^2)u_l^1]\\&=\omega_0^{(\alpha)}u_l^0+\mathrm{i}\beta[\frac{m_0}{\rho_0}(\frac{x_0-x_l}{h})^2W_{0j}u_0^1\\&+\frac{m_{N-1}}{\rho_{N-1}}\left(\frac{x_{N-1}-x_l}{h}\right)^2W_{N-1,j}u_{N-1}^1]-\mathrm{i}f_l^1.\end{aligned}\tag{51}$$

Then we can solve the following system of equations

$$A_lM^1=N_l^1.\tag{52}$$

Step 5: Use the first time layer U_i^1 to obtain the numerical format of the k time layer U_i^k ($k\geq 2$).

Step 6: Repeat Step 5 until the discrete solution of TF-NLSE is obtained for each discrete point (x_i,t_k).

The implicit discrete scheme for the coupled time fractional Schrödinger equation can be obtained analogously.

6. Numerical experiments

In this section, the wide application of the implicit numerical scheme (Eq. (41)) proposed in this paper in solving the fractional nonlinear Schrödinger equation will be verified by going through several numerical experiments. Firstly, we have used the method to solve the coupled time fractional nonlinear Schrödinger equation to determine its feasibility, and verified that the proposed method has a high numerical accuracy for the coupled time fractional nonlinear Schrödinger equation. Secondly, the proposed method is used to solve the time fractional nonlinear Schrödinger equation numerically, and is extended to the irregular region. Meanwhile, compared with other existing numerical methods,[42,46] the effectiveness and accuracy of the proposed method are further verified. We choose the smooth length of the kernel function is selected from $0.9dx$ to $1.2dx$, where dx is the initial particle spacing. The following error criteria are used in this section to compare the difference between numerical results and analytical solutions to measure their accuracy. In this paper, the L_∞, L_2, root-mean-square (RMS) errors, and the convergence order Cr are calculated as follows:[42,46]

$$\begin{aligned}&E_\infty^\phi(\Delta x,\tau)=\max_{1\leq i\leq N}|\phi(u_i^k)-\phi(u(x_i,t_k))|,\\&Cr_\infty^\phi=\log_2\frac{E_\phi(\Delta x,\tau)}{E_\phi(\Delta x/2,\tau)},\\&E_{\mathrm{RMS}}^\phi(\Delta x,\tau)=\sqrt{\frac{1}{N}\sum_{i=1}^{N}|u_i^k-u(x_i,t_k)|^2},\end{aligned}\tag{53}$$

$$E_2^\phi=\sqrt{h\sum_{i=0}^{N-1}\left|u_i^k-u(x_i,t_k)\right|^2},\tag{54}$$

where $h=\Delta x$, $u(x_i,t_k)$ is exact solution of $u(x,t)$ at point (x_i,t_k) and u_i^k is numerical solution. Here, ϕ represents the real, imaginary parts, and module of u, respectively.

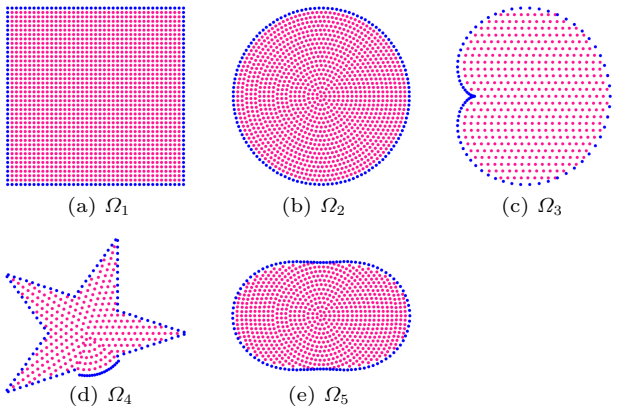


Fig. 1. The simulation region of Ω_i ($i=1,2,3,4,5$) used in this article: (a) Ω_1, (b) Ω_2, (c) Ω_3, (d) Ω_4, and (c) Ω_5.

It is worth noting that figure 1 provides a schematic representation of all the calculation areas employed in this article.

6.1. Solitary wave propagation with identical initial values

In this section, the time step is $\tau=0.001$.

Example 1 We consider the following coupled time fractional Schrödinger equation with the same analytical solution:

$$\begin{cases}\mathrm{i}\,{}_0^CD_t^\alpha u(x,t)+\mathrm{i}u_x+u_{xx}+2u+v=f_1(x,t),\\ \mathrm{i}\,{}_0^CD_t^\alpha v(x,t)-\mathrm{i}v_x+v_{xx}+u-3v=f_2(x,t),\end{cases}$$

the initial condition is

$$u(x,0)=v(x,0)=0.$$

The source term is

$$\begin{cases}f_1(x,t)=\dfrac{2t^{2-\alpha}}{\Gamma(3-\alpha)}\mathrm{e}^{\mathrm{i}\pi x}+t^2\mathrm{e}^{\mathrm{i}\pi x}(3-\pi-\pi^2),\\ f_2(x,t)=\dfrac{2t^{2-\alpha}}{\Gamma(3-\alpha)}\mathrm{e}^{\mathrm{i}\pi x}+(\pi-\pi^2-2)t^2\mathrm{e}^{\mathrm{i}\pi x}.\end{cases}$$

The analytical solution is

$$u(x,t)=t^2\mathrm{e}^{\mathrm{i}\pi x},\quad v(x,t)=t^2\mathrm{e}^{\mathrm{i}\pi x}.$$

Table 1. Comparison of L_∞ error and convergence rate under different α at $t=1, x\in[0,1]$.

L_∞	N	Re(u)	Cr	Im(u)	Cr	$\lvert u\rvert$	Cr
$\alpha=0.9$	21	1.2372×10^{-3}		3.8754×10^{-3}		4.0009×10^{-3}	
	41	3.0942×10^{-4}	1.999	9.6754×10^{-4}	2.001	1.0014×10^{-3}	1.998
	81	7.7310×10^{-5}	2.001	2.4182×10^{-4}	2.000	2.4939×10^{-4}	2.000
	161	1.9330×10^{-5}	2.000	6.0470×10^{-5}	2.000	6.2570×10^{-5}	2.000
$\alpha=0.7$	21	1.1433×10^{-3}		3.8897×10^{-3}		3.9894×10^{-3}	
	41	2.8621×10^{-4}	1.998	9.7109×10^{-4}	2.001	9.9792×10^{-4}	1.999
	81	7.1510×10^{-5}	2.001	2.4269×10^{-4}	2.000	2.4939×10^{-4}	2.001
	161	1.7870×10^{-5}	2.000	6.0680×10^{-5}	2.000	6.2340×10^{-5}	2.000
$\alpha=0.4$	21	1.0050×10^{-3}		3.9212×10^{-3}		3.9864×10^{-3}	
	41	2.5063×10^{-4}	2.004	9.7892×10^{-4}	2.002	9.9623×10^{-4}	2.001
	81	6.2630×10^{-5}	2.001	2.4465×10^{-4}	2.001	2.4901×10^{-4}	2.000
	161	1.5660×10^{-5}	2.000	6.1160×10^{-5}	2.000	6.2250×10^{-5}	2.000

The Dirichlet boundary condition can be obtained by the above analytical solution.

In order to show the accuracy and convergence rate of solving coupled time fractional Schrödinger problem using the scheme proposed in this paper, the L_∞ errors and convergence rate of three different physical quantities of wave function u are listed in Table 1.

From Table 1, it can be seen that (i) the error decreases with the increase of particle number N, and has a faster convergence rate; (ii) the proposed numerical method exhibits high numerical accuracy in the simulation of the coupled time fractional Schrödinger equation.

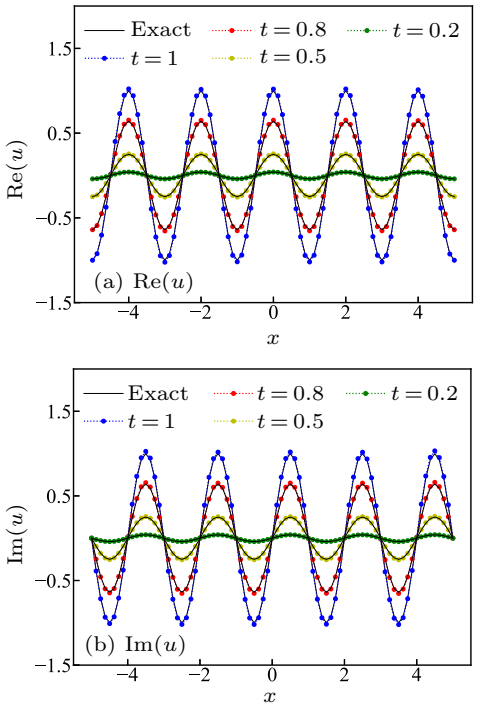


Fig. 2. Comparison diagram between the exact and numerical solutions of the wave function u: (a) Re(u), (b) Im(u).

Figure 2 simulates the changes of the real and imaginary parts of the wave function u over time in the region Ω_1. When compared to the analytic solution, it becomes evident that the numerical simulation results align closely with the analytical predictions. The specific parameters utilized in this simulation are as follows: $\alpha=0.7$, $\tau=0.001$, $x\in[-5,5], t\in[0,1]$. Obviously, we can see that the real part of the wave function u shows a cosine trend, and the imaginary part shows a sine trend.

Example 2 We consider the following non-homogeneous coupled time fractional nonlinear Schrödinger equation in the region Ω_1:

$$\begin{cases} \mathrm{i}\,{}_0^C D_t^\alpha u(x,t)+\mathrm{i}u_x+u_{xx}+u+v+2(|u|^2+|v|^2)u=f_1(x,t),\\ \mathrm{i}\,{}_0^C D_t^\alpha v(x,t)-\mathrm{i}v_x+v_{xx}+u-v+4(|u|^2+|v|^2)v=f_2(x,t). \end{cases}$$

The source term is

$$\begin{cases} f_1(x,t)=-\dfrac{2t^{2-\alpha}}{\Gamma(3-\alpha)}\sin x+4t^6\cos x\\ \qquad\qquad +\mathrm{i}\left(\dfrac{2t^{2-\alpha}}{\Gamma(3-\alpha)}\cos x+4t^6\sin x\right),\\ f_2(x,t)=-\dfrac{2t^{2-\alpha}}{\Gamma(3-\alpha)}\sin x+8t^6\cos x\\ \qquad\qquad +\mathrm{i}\left(\dfrac{2t^{2-\alpha}}{\Gamma(3-\alpha)}\cos x+8t^6\sin x\right). \end{cases}$$

The analytical solutions are

$$u(x,t)=t^2(\cos x+\mathrm{i}\sin x),$$
$$v(x,t)=t^2(\cos x+\mathrm{i}\sin x).$$

The above equations have the computing domain $[0,2\pi]$, $t\in[0,1]$. The periodic boundary condition can be obtained by the above analytical solution. Table 2 records the RMS error of the present numerical method and other numerical methods. As can be seen from Table 2: by comparing the numerical results of the proposed scheme with those of the existing numerical results,[42] it can be seen that the errors of the proposed scheme when taking different particle numbers are much smaller than those obtained by the method in Ref. [42]. Therefore, the reliability of the proposed method is verified by comparisons. Table 3 shows the RMS error generated by the

proposed method in Example 2 at different times, and compares them with the numerical results of the two different methods given in Ref. [42]. It demonstrates the variation of the numerical error over time. Therefore, the proposed method has a smaller error, and the reliability of the proposed method is verified by comparisons.

Table 2. Comparative study of the RMS error in Example 2 at time $t = 1$.

α	N	Re(u)		Im(u)		$\lvert u\rvert$	
		Ref. [42]	Present	Ref. [42]	Present	Ref. [42]	Present
0.7	6		7.3616×10^{-2}		8.7054×10^{-2}		1.1401×10^{-1}
	11		2.4757×10^{-2}		2.8011×10^{-2}		3.7383×10^{-2}
	21	8.4311×10^{-3}	5.0287×10^{-3}	6.5213×10^{-3}	6.0286×10^{-3}	1.0681×10^{-2}	7.8506×10^{-3}
	41	2.2924×10^{-3}	9.5799×10^{-4}	1.7690×10^{-3}	8.2398×10^{-4}	2.8955×10^{-3}	1.2636×10^{-3}

Table 3. Comparative study of RMS error at different values of times.

	Time	Ref. [42] uniform	Ref. [42] local	Present method
RMS	0.1	1.1916×10^{-5}	1.1106×10^{-5}	5.7132×10^{-6}
	0.3	2.1605×10^{-4}	2.0310×10^{-4}	1.0031×10^{-4}
	0.5	7.2793×10^{-4}	7.0922×10^{-4}	3.2462×10^{-4}
	0.8	1.3812×10^{-3}	1.1512×10^{-3}	3.9775×10^{-4}
	1.0	2.8955×10^{-3}	2.5712×10^{-3}	1.2636×10^{-3}

Figure 3 simulates the evolution of the real and imaginary parts of the wave function u in Example 2 at four different times within the region Ω_1, and compares it with the analytical solution. It can be seen that the numerical simulation results are consistent with the analytical solution, and the parameters used are as follows: $\alpha = 0.7$, $\Delta x = 1/40$, $\tau = 0.001$, $x \in [0, 2\pi]$, $t \in [0, 1]$. Obviously, the real part of the wave function u shows a cosine trend, and the imaginary part shows a sine trend.

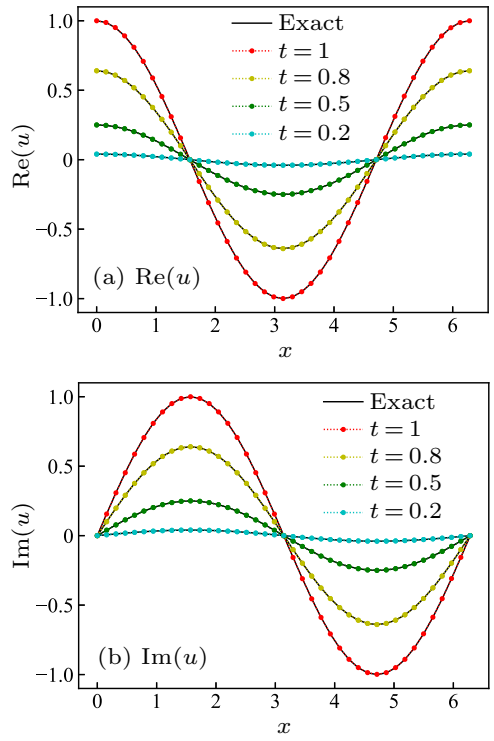


Fig. 3. Simulation results of the curves Re(u) and Im(u) for Example 2 with at different values of time.

6.2. Solitary wave propagation with different initial values

The coupled TF-NLSE equation with periodic boundary without analytical solution is a typical problem in which singular and complex phenomena occur during the propagation of solitary wave. Currently, this equation is often used to verify the reliability of the proposed algorithm to simulate the propagation process of nonlinear solitary waves with periodic boundary. To further demonstrate that the proposed meshless method can accurately capture the complex wave phenomena in the propagation of multi-component solitary waves, we consider in this section the coupled time fractional Schrödinger equation without analytical solution that can describe the inelastic collision process of solitons.

Example 3 We consider the time fractional coupled nonlinear Schrödinger equation without analytical solutions in the region Ω_1:

$$\begin{cases} \mathrm{i}\,{}_0^C D_t^\alpha u(x,t) + u_{xx} + (|u|^2 + 5|v|^2)u = f_1(x,t), \\ \mathrm{i}\,{}_0^C D_t^\alpha v(x,t) + v_{xx} + (|v|^2 + 5|u|^2)u = f_2(x,t), \end{cases}$$

with the initial condition and the periodic boundary condition

$$\begin{cases} u(x,0) = \sqrt{2}\,\mathrm{e}^{\mathrm{i}x/4}\,\mathrm{sech}(x+10), \\ v(x,0) = \sqrt{2}\,\mathrm{e}^{-\mathrm{i}x/4}\,\mathrm{sech}(x-10), \end{cases}$$
$$\begin{cases} u(x,t) = u(x+80,t), \\ v(x,t) = v(x+80,t), \end{cases}$$

where $x \in [-40, 40]$, $t \in [0, 30]$, $f_1 = f_2 = 0$.

Figure 4 shows the numerical prediction results of the solitary wave functions $|u|$ and $|v|$ under different α in region Ω_1. Figure 4 is the numerical simulation results of the proposed method when α=0.5, 0.6, 0.7, and 0.9, respectively. The parameters used are as follows: $x \in [-40, 40]$, $t = 30$, the time step $\tau = 0.1$. Obviously, as can be seen from Fig. 4: (i) In the fractional case, as parameter α increases, the peak values of the solitary wave functions $|u|$ and $|v|$ decrease, and the waves widen. (ii) The soliton height will collapse with the increase of the parameter α, which is a complex propagation phenomenon. (iii) At time $t = 30$, the simulation results align with the finite difference results, indicating a good

agreement between the two. This consistency indicates that the proposed method is reliable for numerically predicting the complex propagation dynamics of nonlinear solitary waves generated by inelastic collisions in fractional order systems. Figure 5 shows the solitary wave propagation phenomenon of coupled TF-NLSE, namely, the wave collapse phenomenon of the fractional solitary wave generated by inelastic collisions, which is similar to the phenomenon in Ref. [28] and more complex than the general phenomenon. According to Figs. 4 and 5, it is further demonstrated that the particle method proposed in this paper is reliable in capturing the strange and complex phenomena in the propagation of nonlinear solitary wave. In summary, the shape changes of nonlinear solitary waves in fractional-order during propagation are more complex, including multimodal structures. The propagation speed and attenuation rate of solitary waves are influenced by the order of fractional derivatives and other parameters, which can lead to different propagation behaviors and evolution patterns.

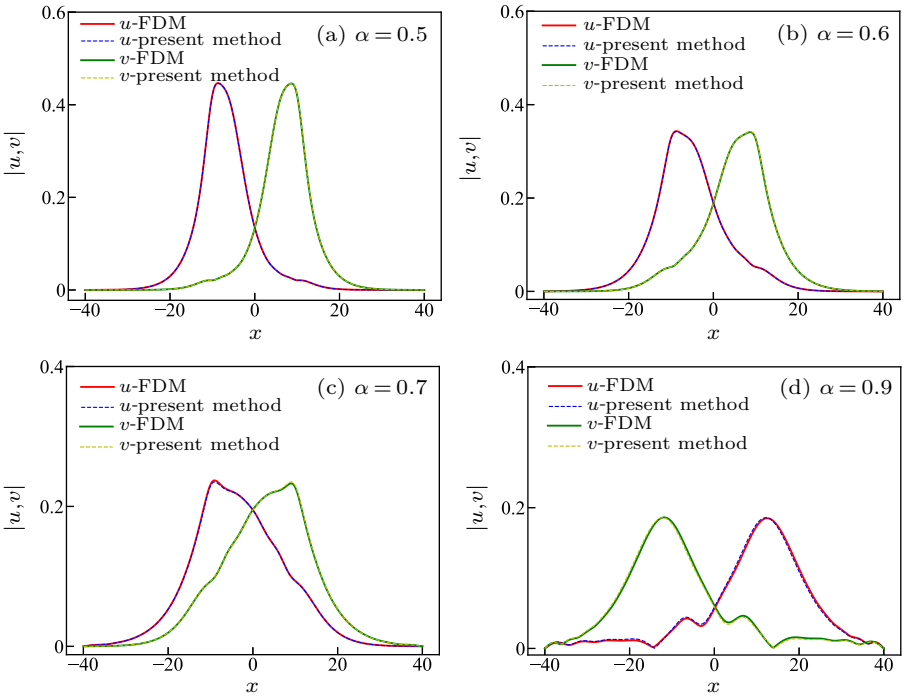


Fig. 4. Comparisons of numerical results for solitary wave function $|u|$ and $|v|$ at $t = 30$: (a) $\alpha = 0.5$, (b) $\alpha = 0.6$, (c) $\alpha = 0.7$, (d) $\alpha = 0.8$.

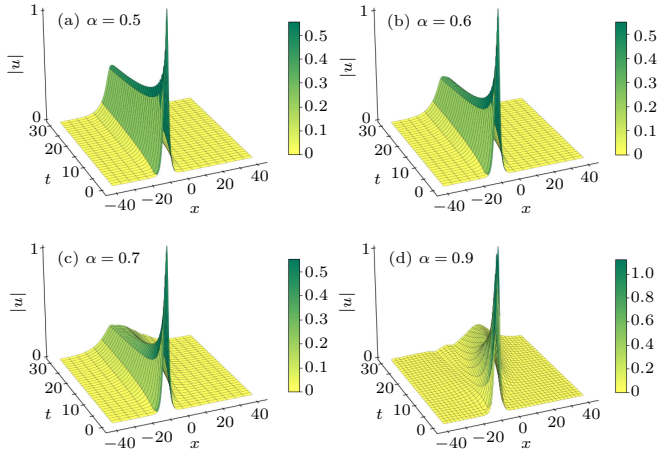


Fig. 5. Surface plots of solitary wave function $|u|$ obtained by the proposed method for different α: (a) $\alpha = 0.5$, (b) $\alpha = 0.6$, (c) $\alpha = 0.7$, (d) $\alpha = 0.8$.

6.3. Solitary wave propagation in regular and irregular regions

In this section, to further demonstrate the advantages of the proposed meshless method, we conducted research on both regular and irregular regions. It highlights that the proposed method in this article can also obtain more accurate numerical solutions and simulation graphs when dealing with complex computational domains. Meanwhile, we discussed examples with and without analytical solutions, demonstrating the flexibility of the proposed meshless method.

Example 4 We consider the time fractional nonlinear Schrödinger equation in the regions Ω_1:

$$\mathrm{i}\frac{\partial^\alpha u(x,t)}{\partial t^\alpha} + \frac{\partial^2 u(x,t)}{\partial x^2} + |u(x,t)|^2 u(x,t) = f(x,t),$$
$$0 \le x \le 1, \quad 0 \le t \le T.$$

The initial condition, the Dirichlet boundary condition, and the function f are

$$u(x,0) = 0, \quad 0 \le x \le 1;$$
$$u(0,t) = 0, \quad u(1,t) = \mathrm{i}t^2, \quad 0 \le t \le T,$$

$$\begin{aligned} & f(x,t) \\ &= -\frac{2t^{2-\alpha}}{\Gamma(3-\alpha)}x^2 - 2t^2 + t^6x^3(1-x)((1-x)^2+x^2) \\ &\quad + \mathrm{i}\left(\frac{(2t^{2-\alpha})}{\Gamma(3-\alpha)}(1-x)x + t^6x^4\left(x^2+(1-x)^2\right) + 2t^2\right). \end{aligned}$$

The analytical solution is

$$u(x,t) = t^2\big((1-x)x + \mathrm{i}x^2\big).$$

In this example, we take the time step as $\tau = 0.001$. For Example 4, we have solved the problem using the proposed method in this paper with various values of τ, where $\alpha = 0.1$, $N = 41$, and $t = 1$. Tables 4 and 5 compare the L_∞ and L_2 errors of our results with the existing numerical results,[46] respectively. It can be observed that our method exhibits higher accuracy in comparison with the method reported in Ref. [46]. Based on Tables 4 and 5, we can conclude that the proposed method achieves better accuracy with only a small number of particles. In addition, the accuracy of the present method is superior to the existing numerical results,[46] thus validating the validity and accuracy of the numerical method.

Figure 6 presents the numerical solutions for the real and imaginary parts, along with the absolute error distribution plots, respectively. Figure 7 compares the error distribution plots between the present method and the method described in Ref. [46], considering the parameters $\alpha = 0.1$, $\Delta x = 1/40$, $t = 1$, and $\tau = 1/256$. From this comparison, it is evident that the present method exhibits smaller errors compared to the method in Ref. [46], highlighting the superiority of the proposed method.

Table 4. Comparative study on the L_∞ error at $\Delta x = 1/40$, $\alpha = 0.1$, $t = 1$.

α	τ	Ref. [46]		Present method	
		Re(u)	Im(u)	Re(u)	Im(u)
0.1	1/16	1.69582×10^{-2}	1.64917×10^{-2}	7.1346×10^{-4}	3.1322×10^{-3}
	1/32	8.50622×10^{-3}	8.22627×10^{-3}	3.7785×10^{-4}	1.6563×10^{-3}
	1/64	4.26873×10^{-3}	4.11967×10^{-3}	1.9457×10^{-4}	8.5218×10^{-4}
	1/128	2.1514×10^{-3}	2.07201×10^{-3}	9.8744×10^{-5}	4.3229×10^{-4}
	1/256	1.0934×10^{-3}	1.05034×10^{-3}	4.9744×10^{-5}	2.1772×10^{-4}
	1/512	5.64571×10^{-4}	5.40111×10^{-4}	2.4966×10^{-5}	1.0926×10^{-4}

Table 5. Comparative study on the L_2 error at $\Delta x = 1/40$, $\alpha = 0.1$, $t = 1$.

α	τ	Ref. [46]		Present method	
		Re(u)	Im(u)	Re(u)	Im(u)
0.1	1/16	1.23434×10^{-2}	6.1227×10^{-2}	4.9027×10^{-4}	2.1580×10^{-3}
	1/32	6.19172×10^{-3}	6.09586×10^{-3}	2.5961×10^{-4}	1.1413×10^{-3}
	1/64	3.10742×10^{-3}	3.0518×10^{-3}	1.3367×10^{-4}	5.8722×10^{-4}
	1/128	1.56613×10^{-3}	1.5346×10^{-3}	6.7837×10^{-5}	2.9789×10^{-4}
	1/256	7.95972×10^{-4}	7.77774×10^{-4}	3.4173×10^{-5}	1.5004×10^{-4}
	1/512	4.11009×10^{-4}	3.99849×10^{-4}	1.7151×10^{-5}	7.5293×10^{-5}

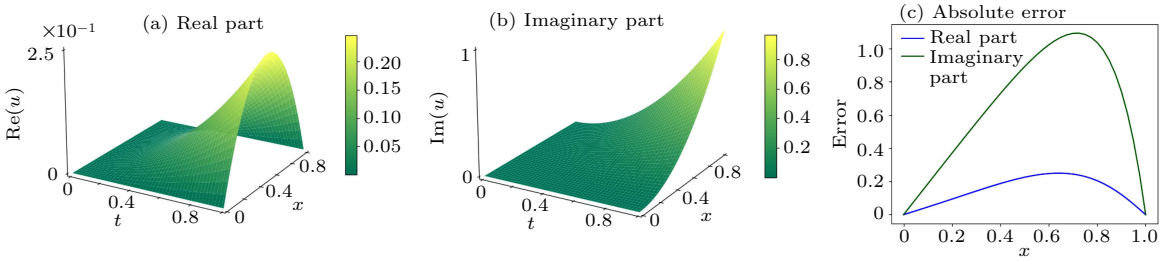


Fig. 6. Numerical solutions and the error curves of the real and imaginary parts for $\alpha = 0.1$, $\tau = 1/512$, and $\Delta x = 1/40$: (a) real part, (b) imaginary part, (c) absolute error.

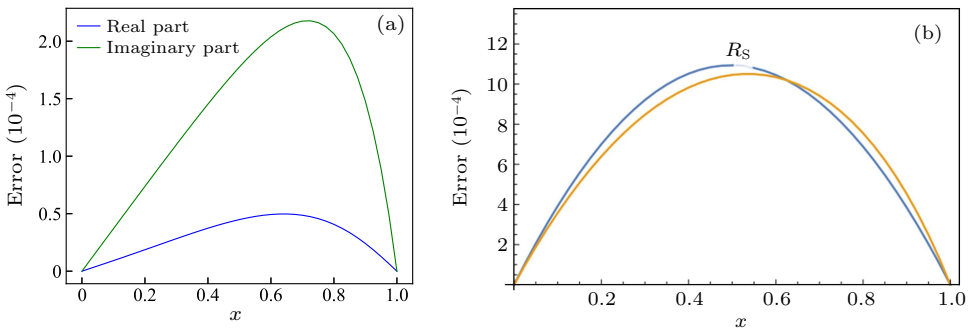


Fig. 7. Error curves of the real and imaginary parts in Example 4 for $\alpha = 0.1$, $\Delta x = 1/40$, $t = 1$, $\tau = 1/256$: (a) the present method and (b) Ref. [46].

Example 5 We consider the 2D time fractional nonlinear Schrödinger equation in the irregular regions Ω_3:

$$\mathrm{i}\,{}_0^C D_t^\alpha u(x,y,t) - u_{xx} - u_{yy} + |u|^2 u = f(x,y,t), \quad t \geq 0.$$

The initial condition, the Dirichlet boundary conditions and the source term f are respectively given by

$$\begin{aligned} u(x,y,0) &= 0, \quad u(x,y,t) = m(x,y,t), \quad (x,y) \in \partial\Omega, \\ f(x,y,t) &= (1+\mathrm{i})\Big[2t^2(y(1-y)+x(1-x)) \\ &\quad + \mathrm{i}(1-x)(1-y)xy\frac{2t^{2-\alpha}}{\Gamma(3-\alpha)} \\ &\quad + 2t^6(1-x)^3(1-y)^3x^3y^3\Big]. \end{aligned}$$

The analytical solution is $u(x,y,t) = (1+\mathrm{i})t^2(1-x)(1-y)xy$. The function $m(x,y,t)$ can be given by analytical solution. For Example 5, we take the time step of $\tau = 0.01$. In Table 6, the numerical results of the L_∞ error generated by the proposed method in the irregular region Ω_3 at time $t = 1$. As can be seen from Table 6: (i) The error of this method decreases with the increase of particle number N. (ii) It can be seen from the data that the error obtained by the present method is relatively small. This indicates that the proposed method is accurate and exhibits good agreement with the analytical solution. The results also show that the proposed method can be used to deal with the 2D nonlinear fractional Schrödinger problem in the irregular region, and the applicability of the proposed method is also verified.

Table 6. The L_∞ error of the proposed method at $t = 1$ in Ω_3.

α	N	Present method		
		Re(u)	Im(u)	$\lvert u\rvert$
0.3	34	2.3655×10^{-2}	2.3356×10^{-2}	3.3241×10^{-2}
	102	1.1422×10^{-2}	1.1369×10^{-2}	1.6115×10^{-2}
	358	7.0579×10^{-3}	7.0456×10^{-3}	9.9727×10^{-3}
	1312	3.3100×10^{-3}	3.3071×10^{-3}	4.6790×10^{-3}
	5044	1.7928×10^{-3}	1.7916×10^{-3}	2.5345×10^{-3}

Figure 8 shows the numerical simulation results obtained by the method described in this paper at different moments, with the parameters $\alpha = 0.3$ and $N = 5044$. By comparing the migration and diffusion processes of the solitary wave at time instances $t = 0.6, 0.8, 0.9, 1.5$, it is evident from Fig. 8 that the solitary wave gradually diffuses from the periphery towards the center, with the wave peak continuously shifting.

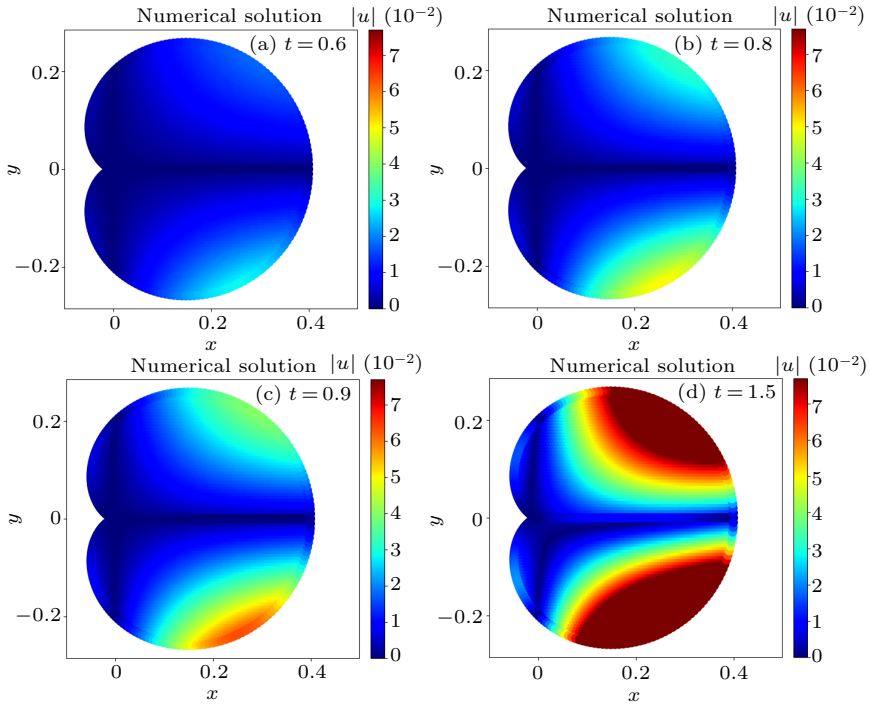


Fig. 8. Cloud diagram of the solitary wave function $|u|$ obtained by the present method at different values of time: (a) $t = 0.6$, (b) $t = 0.8$, (c) $t = 0.9$, and (d) $t = 1.5$.

Example 6 Consider the 2D time fractional nonlinear Schrödinger equation in the regions Ω_2 and Ω_4:

$$\mathrm{i}\,{}_0^C D_t^\alpha u(x,y,t) + u_{xx} + u_{yy} + |u|^2 u = f(x,y,t).$$

The source term is

$$\begin{aligned} f(x,t) &= t^{3\alpha+3}\left(\frac{1}{64}\sin^2(2\pi x)\sin^2(\pi y)\right. \\ &\quad \left. + \frac{1}{144}\sin^2(\pi x)\sin^2(2\pi y)\right) \\ &\quad \times \left(\frac{1}{8}\sin(2\pi x)\sin(\pi y) + \frac{\mathrm{i}}{12}\sin(\pi x)\sin(2\pi y)\right) \\ &\quad + t\left(\sin(2\pi x)\sin(\pi y)\left(\frac{\mathrm{i}\Gamma(\alpha+2)}{8} - \frac{5\pi^2 t^\alpha}{8}\right)\right. \end{aligned}$$

$$-\sin(\pi x)\sin(2\pi y)\left(\frac{\Gamma(\alpha+2)}{12}-\frac{5\mathrm{i}\pi^2 t^{\alpha}}{12}\right)\Bigg). \quad (55)$$

The analytical solution is

$$u(x,y,t) = t^{\alpha+1}\sin(2\pi x)\sin(\pi y) \times\left(\frac{\mathrm{i}}{6}\cos(\pi y)+\frac{1}{4}\cos(\pi x)\right).$$

The initial and boundary conditions of this numerical example can all be given analytically through the analytical solution. For Example 6, we take the time steps of $\tau = 0.01$.

Table 7 records the L_∞ error and convergence rate obtained by the present method when different α values are selected. The data shows that this method has high convergence accuracy. As can be seen from Table 8: (i) The calculation error of the method decreases with the increase of particle number N. In other words, as the number of particles increases, the precision of the numerical solution increases significantly. (ii) By observing the above numerical results, it is evident that the proposed scheme exhibits a small error for varying particle numbers, thereby confirming its reliability in addressing the 2D time fractional nonlinear Schrödinger equation. Additionally, it shows the reliability of the numerical prediction of the proposed scheme on the irregular region Ω_4.

Table 7. The L_∞ error and convergence rate of the proposed method for different α at $t = 1$ in Ω_1.

α	N	Present method					
		Re(u)	Cr	Im(u)	Cr	$\lvert u\rvert$	Cr
0.3	36	1.4970×10^{-2}		1.0071×10^{-2}		1.5344×10^{-2}	
	121	3.7070×10^{-3}	2.014	2.4785×10^{-3}	2.023	3.7364×10^{-3}	2.038
	441	9.4065×10^{-4}	1.979	6.3435×10^{-4}	1.966	9.4066×10^{-4}	1.990
	1681	2.1230×10^{-4}	2.148	1.4872×10^{-4}	2.093	2.1230×10^{-4}	2.148
0.6	36	1.4990×10^{-2}		1.0104×10^{-2}		1.5342×10^{-2}	
	121	3.7065×10^{-3}	2.016	2.4782×10^{-3}	2.028	3.7360×10^{-3}	2.038
	441	9.4057×10^{-4}	1.978	6.3428×10^{-4}	1.966	9.4057×10^{-4}	1.990
	1681	2.1231×10^{-4}	2.147	1.4880×10^{-4}	2.092	2.1231×10^{-4}	2.147
0.9	36	1.5022×10^{-2}		1.0154×10^{-2}		1.5340×10^{-2}	
	121	3.7062×10^{-3}	2.019	2.4779×10^{-3}	2.035	3.7358×10^{-3}	2.038
	441	9.4058×10^{-4}	1.978	6.3426×10^{-4}	1.966	9.4059×10^{-4}	1.990
	1681	2.1242×10^{-4}	2.147	1.4894×10^{-4}	2.090	2.1244×10^{-4}	2.146

Table 8. The L_∞ error of the proposed method for different α in Ω_4.

α	N	Present method		
		Re(u)	Im(u)	$\lvert u\rvert$
0.3	151	2.4265×10^{-3}	2.7153×10^{-3}	2.2753×10^{-3}
	508	1.3092×10^{-3}	1.3956×10^{-3}	1.4459×10^{-3}
	1809	5.9148×10^{-4}	6.7798×10^{-4}	7.1597×10^{-4}
	6777	3.2901×10^{-4}	3.3268×10^{-4}	3.3454×10^{-4}
0.5	151	1.7597×10^{-3}	1.9678×10^{-3}	1.6531×10^{-3}
	508	9.4918×10^{-4}	1.0110×10^{-3}	1.0478×10^{-3}
	1809	4.2872×10^{-4}	4.9130×10^{-4}	5.1889×10^{-4}
	6777	2.3783×10^{-4}	2.4106×10^{-4}	2.5632×10^{-4}
0.8	151	1.0876×10^{-3}	1.2139×10^{-3}	1.0250×10^{-3}
	508	5.8621×10^{-4}	6.2307×10^{-4}	6.4623×10^{-4}
	1809	2.6460×10^{-4}	3.0306×10^{-4}	3.2015×10^{-4}
	6777	1.4652×10^{-4}	1.4875×10^{-4}	1.6208×10^{-4}

Figure 9 simulates the propagation cloud image of the solitary wave $|u|$ and its corresponding error in the region Ω_4, with the parameters set to $t = 0.2$ and $N = 1809$. Obviously, as can be seen from Figure 9: (i) Figure 9(a) demonstrates that, in the fractional order case, the solitary wave function $|u|$ attains its peak near the edge, with the lowest wave height occurring at the center. Furthermore, the figure shows the evolution of waves over time. (ii) Figure 9(b) demonstrates that the error of the solitary wave function $|u|$ obtained using the format proposed in this paper is very small, up to 10^{-4}. This indicates that the meshless particle method proposed in this paper is reliable and accurate for numerically predicting the time fractional Schrödinger model in the irregular region Ω_4.

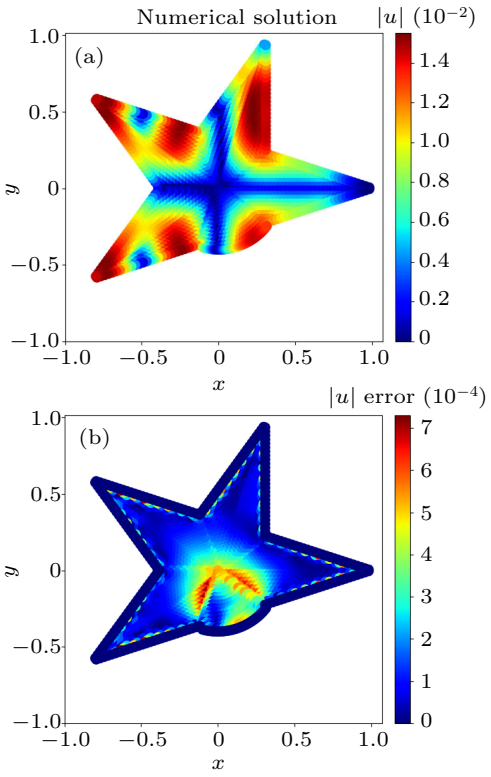


Fig. 9. Numerical solution and error cloud plots for $|u|$ at $\alpha = 0.3$ in Example 6: (a) numerical solution of $|u|$ and (b) error of $|u|$.

Table 9 gives the numerical results of the L_∞ errors pro-

duced by this method for the three physical quantities of u when taking different numbers of particles in the irregular region Ω_2 at $t = 0.2$. As can be seen from Table 9: (i) The errors of the three physical quantities obtained using the method described in this paper decrease as the number of particles N increases. (ii) We found that the numerical results generated by our method for different particle numbers have very small errors in Ω_2, reaching 10^{-5}. This not only verifies the feasibility of the proposed method for solving the 2D nonlinear fractional Schrödinger equation over time but also demonstrates its reliability for numerically predicting isolated wave experiments in the irregular region Ω_2.

Table 9. The L_∞ error of the proposed method for different α in Ω_2.

α	N	Present method		
		Re(u)	Im(u)	$\lvert u\rvert$
0.3	24	1.9327×10^{-3}	1.2051×10^{-3}	1.9330×10^{-3}
	351	5.1797×10^{-4}	3.3311×10^{-4}	5.1797×10^{-4}
	1330	3.8426×10^{-4}	2.5209×10^{-4}	3.8426×10^{-4}
	5173	2.1965×10^{-4}	1.4318×10^{-4}	2.1965×10^{-4}
0.5	24	1.3938×10^{-3}	8.9762×10^{-4}	1.3944×10^{-3}
	351	3.7541×10^{-4}	2.4162×10^{-4}	3.7541×10^{-4}
	1330	2.7849×10^{-4}	1.8278×10^{-4}	2.7849×10^{-4}
	5173	1.5917×10^{-4}	1.0382×10^{-4}	1.5917×10^{-4}
0.8	24	8.4173×10^{-4}	5.9803×10^{-4}	8.4321×10^{-4}
	351	2.3164×10^{-4}	1.4941×10^{-4}	2.3164×10^{-4}
	1330	1.7179×10^{-4}	1.1289×10^{-4}	1.7179×10^{-4}
	5173	9.8182×10^{-5}	6.4149×10^{-5}	9.8182×10^{-5}

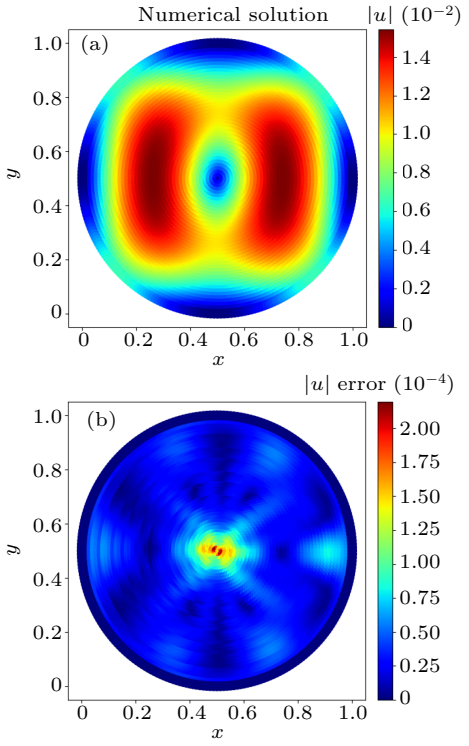


Fig. 10. The cloud diagram of numerical solution and error for $|u|$ at $\alpha = 0.3$ in Example 6: (a) numerical solution of the isolated wave function $|u|$, (b) error of the isolated wave function $|u|$.

Figure 10 simulates the propagation cloud image of the solitary wave $|u|$ in Example 6 when $t = 0.2$ and $N = 5173$ as the relevant parameters. It also illustrates the corresponding error cloud image in the irregular region Ω_2. Obviously, as can be seen from Fig. 10: (i) Figure 10(a) shows that two symmetrical peaks are formed in the Ω_2 region. In addition, the waves spread around and the peaks gradually decrease. The center presents a circular shape, and as it approaches the center, the peak gradually decreases to form a trough of wave. (ii) Figure 10(b) shows that the error of the solitary wave function $|u|$ obtained using the method described in this paper is very small, reaching 10^{-5} at $\alpha = 0.8$. In summary, we can see from Fig. 10 that the propagation and collision of solitary waves in nonlinear media may lead to local concentration or diffusion of energy. The nonlinear characteristics of solitary waves may result in complex waveform transformations during collisions. These nonlinear effects result in the formation of a symmetrical ring at the center of the collision, as a result of nonlinear interactions. The numerical results indicate that the proposed method is effective and feasible for solving the time fractional nonlinear Schrödinger equation in irregular regions.

Example 7 Consider the 2D time fractional nonlinear Schrödinger equation in the region Ω_5:

$$\mathrm{i}\,{}_0^C D_t^\alpha u(x,y,t) - u_{xx} - u_{yy} + |u|^2 u = f(x,y,t). \tag{56}$$

The source term is

$$\begin{aligned} f(x,t) \;=\; & \mathrm{i}\frac{2t^{2-\alpha}}{\Gamma(3-\alpha)}\sin(x+y) + 2t^2\sin(x+y) \\ & + t^2|t^2\sin(x+y)|^2\sin(x+y). \end{aligned} \tag{57}$$

The analytical solution is

$$u(x,y,t) = t^2\sin(x+y). \tag{58}$$

The initial and boundary conditions of this numerical example can all be given analytically through the analytical solution. For Example 7, we take the time steps of $\tau = 0.01$.

Table 10. The L_∞ error of the proposed method for different α at $t = 1$ in Ω_5.

α	N	Present method		
		Re(u)	Im(u)	$\lvert u\rvert$
0.3	72	3.7263×10^{-2}	2.7321×10^{-4}	3.7262×10^{-2}
	248	2.3038×10^{-2}	5.9822×10^{-5}	2.3039×10^{-2}
	904	1.4029×10^{-2}	3.1668×10^{-5}	1.4029×10^{-2}
	3472	8.1244×10^{-3}	2.6515×10^{-5}	8.1244×10^{-3}
	13583	4.7873×10^{-3}	2.5077×10^{-5}	4.7874×10^{-3}
0.8	72	3.7263×10^{-2}	3.6874×10^{-4}	3.7262×10^{-2}
	248	2.3039×10^{-2}	7.5014×10^{-5}	2.3039×10^{-2}
	904	1.4029×10^{-2}	5.1939×10^{-5}	1.4029×10^{-2}
	3472	8.1245×10^{-3}	4.8227×10^{-5}	8.1245×10^{-3}
	13583	4.7873×10^{-3}	4.7895×10^{-5}	4.7873×10^{-3}

Table 10 shows the numerical results of the L_∞ error generated by the proposed method for different particle numbers at $t = 1$ in the region Ω_5. As can be seen from Table 10: (i) The calculation error obtained by the method in this paper decreases with the increase of particle number N. (ii) It can be seen that the error of the proposed method is very small when different particle numbers are taken. Consequently, this demonstrates the reliability of the proposed scheme for numerically predicting the time fractional nonlinear Schrödinger model in the 2D irregular region Ω_5.

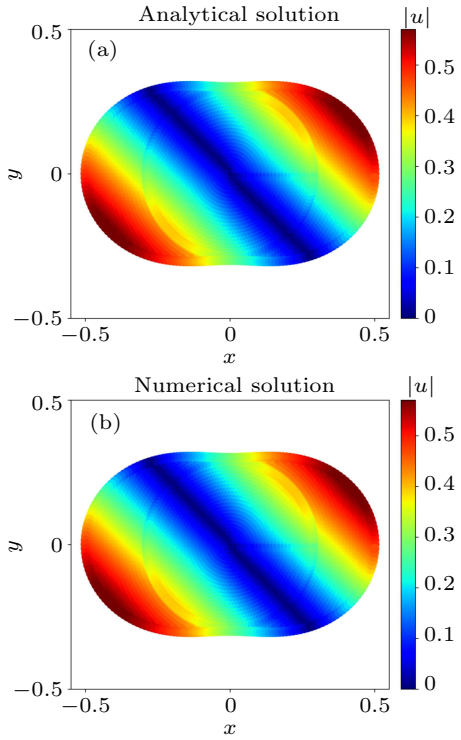


Fig. 11. Cloud diagram of $|u|$ obtained by the present method for Example 7 with $\alpha = 0.8$ at time $t = 1$: (a) analytical solution, (b) numerical solution.

Figure 11 compares the cloud diagram of the numerical solution and the exact solution of the solitary wave $|u|$ in the irregular region Ω_5 when $\alpha = 0.8$, with the parameters set to $t = 1$ and $N = 3472$. In addition, figure 11 shows that in the Ω_5 region, two centrally symmetric solitary wave peaks with equal peak values appear. The wave pattern spreads towards the center, forming a trough. It can also be observed from Fig. 11 that the numerical solution for the solitary wave function $|u|$ obtained using the proposed scheme aligns well with the exact solution depicted in the cloud diagram. This indicates that the method introduced in this article is reliable and accurate for the numerical prediction of the time fractional Schrödinger equation in the irregular region Ω_5. In summary, solitary waves maintain their total energy during collisions. Therefore, as shown in Fig. 11, the nonlinear characteristics of solitary waves may result in complex waveform transformations during collisions. Due to nonlinear interactions, these nonlinear effects result in the formation of complex features.

Example 8 Consider the 2D time fractional nonlinear Schrödinger equation without analytical solution in the region Ω_1:

$$\mathrm{i}\,{}_0^C D_t^\alpha u(x,y,t) + u_{xx} + u_{yy} + |u|^2 u = 0. \tag{59}$$

The initial and boundary conditions are as follows:

$$\begin{aligned} &u(x,y,0) = \sin x \sin y + 2\sin x + \sin y + 2, \\ &u(x,y,t) = u(x+2\pi, y+2\pi, t), \\ &(x,y) \in [0,2\pi] \times [0,2\pi], \quad t \geq 0. \end{aligned} \tag{60}$$

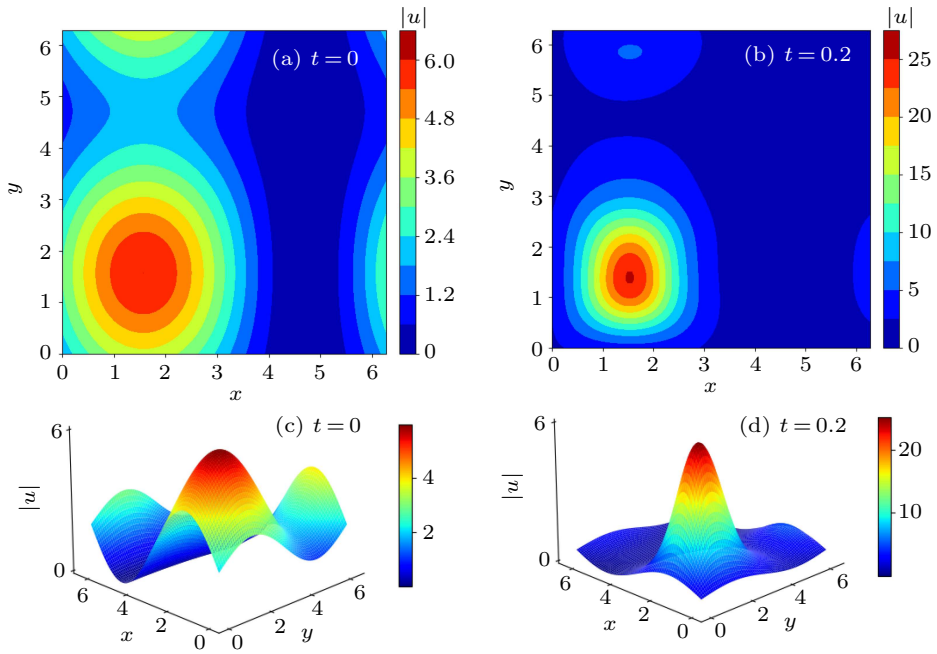


Fig. 12. Waveforms of $|u|$ obtained by this method at different times when $\alpha = 0.9$: (a) $t = 0$, (b) $t = 0.2$, (c) $t = 0$, (d) $t = 0.2$.

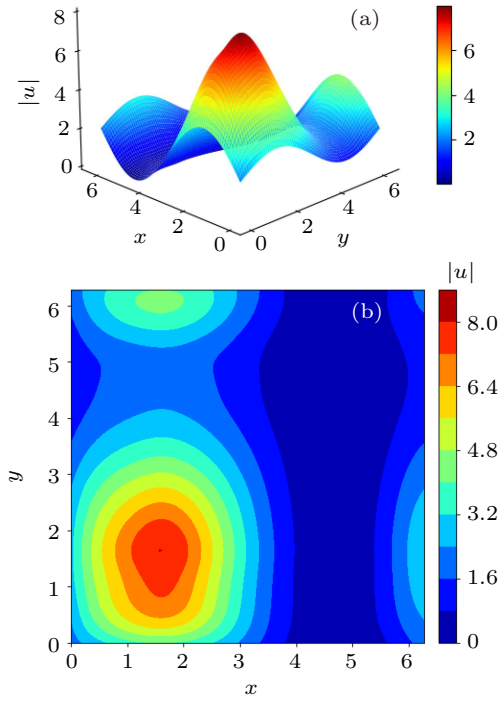


Fig. 13. Simulation diagram of wave function $|u|$ obtained for fractional order: (a) the present method with $\alpha = 0.9$ and (b) $\alpha = 0.9$.

Setting $\tau = 0.01$, we provide a simulation diagram of the numerical solution in Fig. 12. Over time, nonlinear solitary waves undergo merging, resulting in waveform changes and an increase in peak values. Therefore, the phenomena generated by complex fluctuation processes were predicted. From Fig. 13, as time increases, solitary waves begin to split and exhibit dispersion phenomena. At $t = 0.108$, the singularity of the solution at integer order (forming a distinct peak) can be observed through Ref. [47], while this phenomenon is found to diminish at fractional order through the simulations in this paper. This predicts the nonlinear dispersion phenomenon that occurs during the propagation of nonlinear solitary waves under the influence of time memory, which is different from the nonlinear phenomenon under integer order.[47] In summary, the fractional parameter has a significant impact on the fluctuation phenomenon of the TF-NLSE equation.

7. Conclusions and prospect

In this paper, a meshless particle method based on SPH approximation is used to numerically solve the time fractional nonlinear Schrödinger equation and study the complex physical phenomena generated by solitary wave propagation. In numerical research and application, coupled TF-NLSE and general TF-NLSE have been simulated and calculated on different domains. Through validation, the present method exhibits small errors in both regular and irregular regions. In particular, the method is able to achieve high numerical accuracy within the regular region when dealing with time fractional Schrödinger problems. In addition, to further validate the superiority of the proposed method, we compared the numerical results obtained using this method with the results in Refs. [42,46], and it is evident that our method exhibits significantly smaller errors. The detailed comparison results have been shown in Tables 2–5. Based on all numerical results, the method proposed in this paper exhibits significantly smaller errors, therefore effectively addressing solitary wave problems. This not only verifies the effectiveness of the method but also analyzes its error and convergence speed, further highlighting its flexibility. To further validate the effectiveness of our method in practical problems, we simulated and analyzed the phenomenon of fractional solitary wave propagation, as shown in Examples 3 and 8. Based on the above analysis, the method proposed in this article can accurately predict the propagation phenomenon of solitary waves and the complex propagation process caused by inelastic collisions of solitary waves under fractional conditions. In summary, compared with other existing numerical methods, the proposed method has smaller errors and is more accurate in solving the time fractional Schrödinger equation. It provides an effective meshless particle method for predicting complex physical phenomena of fractional solitary wave propagation, with certain advantages, flexibility, and wide applicability.

The theoretical stability and convergence of the meshless particle method proposed in this paper will be further studied in the following work. Meanwhile, we will further investigate the reliability of our method for higher dimensional mathematical models in the future.

Acknowledgement

Project supported by the Natural Science Foundation of Xinjiang Uygur Autonomous Region, China (Grant No. 2024D01C44).

References

[1] Wu Q and Huang J H 2016 *Fractional Calculus* (Beijing: Tsinghua University Press) (in Chinese)
[2] Dehghan M, Manafian J and Saadatmandi A 2010 *Numer. Meth. Partial Differ. Equ.* **24** 448
[3] Rialland G 2024 *Nonlinear Anal.* **241** 113474
[4] Zhou S and Cheng X 2010 *Math. Comput. Simulat.* **80** 2362
[5] Wang X M, Zhang L L and Hu X X 2020 *Optik* **219** 164989
[6] Diethelm K and Ford N J 2002 *J. Math. Anal. Appl.* **265** 229
[7] Sun Z Z and Gao G H 2020 *Fractional Differential Equations: Finite Difference Methods* (Germany: De Gruyter)
[8] Laskin N 2002 *Phys. Rev. E* **66** 056108
[9] Naber M 2004 *J. Math. Phys.* **45** 3339
[10] Amore P, Fernández F M and Hofmann C P 2010 *J. Math. Phys.* **51** 122101
[11] Khoso A I, Katbar M N and Akram U 2023 *Quantum Rep.* **5** 546
[12] Shi L and Zhou X 2022 *Results Phys.* **42** 105967
[13] Mohebbi A ,Abbaszadeh M and Dehghan M 2013 *Eng. Anal. Bound. Elem.* **37** 475
[14] Laskin N 2000 *Phys. Rev. E* **62** 3135
[15] Mao Z P and Karniadakis G E 2018 *SIAM J. Numeri. Anal.* **56** 24

[16] Shivanian E and Jafarabadi A 2017 *Numer. Methods Partial Differ. Equ.* **33** 1043
[17] Alrebdi T A, Arshed S and Raza N 2023 *Results Phys.* **52** 106809
[18] Wang X M, Zhang L L and Hu X X 2020 *Optik* **219** 164989
[19] Ma W X 2022 *Chin. Phys. Lett.* **39** 100201
[20] Eskar R, Feng X and Kasim E 2020 *Adv. Differ. Equ.* **2020** 492
[21] Chen X, Di Y and Duan J 2018 *Appl. Math. Lett.* **84** 160
[22] Dehghan M and Mirzaei D 2008 *Eng. Anal. Bound. Elem.* **32** 747
[23] Liaqat M I and Akgül A 2022 *Chaos, Solitons and Fractals* **162** 1043
[24] Mardani A, Hooshmandasl M R and Heydari M H 2017 *Comput. Math. Appl.* **75** 122
[25] Xu Y, Sun H G and Zhang Y 2023 *Comput. Math. Appl.* **142** 107
[26] Wong A Y and Cheung P Y 1984 *Phys. Rev. Lett.* **52** 1222
[27] Klein C, Sparber C and Markowich P 2014 *Proceedings of the Royal Society A: Math., Phys. Eng. Sci.* **470** 20140364
[28] Chen M, Zeng S and Lu D 2018 *Phys. Rev. E* **98** 022211
[29] Yao Y, Yi H and Zhang X 2023 *Chin. Phys. Lett.* **40** 100503
[30] Qin Z 2022 *Chin. Phys. Lett.* **39** 010501
[31] Zhou S and Cheng X 2010 *Math. Comput. Simulat.* **80** 2362
[32] Wei L, Zhang X and Kumar S 2012 *Comput. Math. Appl.* **64** 2603
[33] Hu H Z, Chen Y P and Zhou J W 2024 *J. Comput. Math.* **42** 1124
[34] Jiang T, Jiang R R and Huang J J 2021 *Chin. Phys. B* **30** 194
[35] Abbaszadeh M, Azis M I and Dehghan M 2024 *Eng. Anal. Bound. Elem.* **169** 105932
[36] Heydari M H, Hosseininia M and Atangana A 2020 *Eng. Anal. Bound. Elem.* **120** 166
[37] Okposo N I, Veeresha P and Okposo E N 2022 *Chin. J. Phys.* **77** 965
[38] Jiang T, Liu Y H, Li Q, Ren J L and Wang D S 2024 *Comput. Phys. Commun.* **296** 109023
[39] Abbas K, Yuma S, Chun Lee Antonio G, Hitoshi G and Javier B 2024 *Comput. Part. Mech.* **11** 1055
[40] Xu X Y, Cheng J, Peng S and Yu P 2024 *Eng. Anal. Bound. Elem.* **158** 473
[41] Hosseini K, Hincal E and Obi O A 2023 *Opt. Quant. Electron.* **55** 599
[42] Li Y, Jiang R R and Jiang T 2022 *Appl. Math. Mech.* **43** 1016 (in Chinese)
[43] Mokhtari R and Mostajeran F 2020 *Commun. Appl. Math. Comput.* **2** 1
[44] Feng D Y and Imin R 2023 *Results Appl. Math.* **17** 100355
[45] Yang X F, Peng S L and Liu M B 2014 *Appl. Math. Model.* **38** 3822
[46] Hadhoud A R, Rageh A A M and Radwan T 2022 *Fractal Fract.* **6** 127
[47] Wang T, Guo B and Xu Q 2013 *J. Comput. Phys.* **243** 382
[48] Sun Z and Wu X 2006 *Appl. Numer. Math.* **56** 193
[49] Gao G, Sun Z and Zhang H 2014 *J. Comput. Phys.* **259** 33
[50] Liu G R and Liu M B 2003 *Smoothed particle hydrodynamics: a meshfree particle method* (Singapore: World Scientific)